Determination of the Recovery Time of Silicon Photomultipliers

submitted by

Patrick Hallen

patrick.hallen@rwth-aachen.de

Bachelor's Thesis in Physics

presented to

Faculty of Mathematics, Computer Science and Natural Sciences
at RWTH Aachen University

in September 2011

made at

III. Physical Institute A

supervised by

Prof. Dr. Thomas Hebbeker
Dr. Markus Merschmeyer

Abstract

This thesis describes the determination of the recovery time of different silicon photomultipliers. The experimental setup uses two LEDs to first fire all the pixels of the SiPM and then probe the recovery process with a second identical light pulse. The SiPM recovers with an exponential process with two time constants. The recharge of the pixels attributes to the dominating fast time constant and the recharge of the bulk attributes to the slow time constant, which dominates the tail of the recovery. The pixel recovery time is approximately between 7 ns and 50 ns and is smaller for small pixel sizes. The bulk recovery time is between approximately 100 ns and 200 ns and is more dominant for a large pixel size. An increase of the recovery time as a function of the overvoltage has been observed.

Zusammenfassung

Diese Arbeit beschreibt die Bestimmung der Erholungszeit von verschiedenen Silizium-Photomultipliern. Der experimentelle Aufbau benutzt dazu zwei LEDs, um erst alle Pixel des SiPMs auszulösen, um dann mit einem zweiten, identischen Lichtpuls den Erholungsvorgang des SiPMs zu untersuchen. Der Erholungsprozess des SiPMs folgt einem exponentiellen Modell mit zwei Zeitkonstanten. Die schnelle und dominierende Zeitkonstante kann dem Aufladevorgangs der einzelnen Pixel zugeordnet werden. Die langsame Zeitkonstante dominiert die letzten 10% der Erholung und kann dem Aufladen des SiPM-Substrats zugeordnet werden. Die Pixel-Erholungszeit liegt zwischen ungefähr 7 ns und 50 ns und nimmt mit kleiner werdenden Pixelgrößen ab. Die langsame Erholungszeit liegt zwischen ungefähr 100 ns und 200 ns und hat einen größeren Einfluss auf die Erholung bei großen Pixeln. Die Erholungszeit nimmt mit steigender Betriebsspannung des SiPMs zu.

Contents

Contents

1. Introduction

Photodetectors play a crucial role in many particle physics experiments as light is often used for an indirect measurement of primary high-energy particles. When a particle passes through matter there are several processes which emit light. For instance there is scintillation which is often used by particle detectors at particle accelerators. Nuclear medicine imaging uses scintillators and photodetectors as well in positron emission tomography (PET).

Photodetectors are used to measure Cherenkov radiation by many astroparticle physics experiments, e.g. the Pierre Auger Observatory and the IceCube Neutrino Observatory. The Pierre Auger Observatory uses also photodetectors for a fluorescence telescope, which observes cosmic ray induced air showers.

Another example is transition radiation which is often used to distinguish between different primary particles as for example by the Transition Radiation Detector (TRD) of the Alpha Magnetic Spectrometer (AMS-02) on the ISS.

Therefore, developing and understanding photodetectors is crucial for experimental particle physics, In this thesis I will investigate the relatively new Silicon Photomultiplier (SiPM), which is a small and high gain photodetector for small light fluxes, which is meant to partly replace the well-established photomultiplier tubes (PMTs). The goal of this thesis is to determine the recovery time of silicon photomultipliers.

1.1. Introduction to Semiconductor Photodetectors

There are several books and papers which give a thorough introduction to semiconductor physics and detectors and which were used as references for this section [1, 2, 3, 4, 5].

A silicon photomultiplier is made of doped silicon, as the name indicates, and belongs therefore to the class of a semiconductor photodetectors. Although there is a wide range of semiconductor photodetectors, they all have the same basic functionality, so the physics of light detection with doped semiconductors will be briefly explained first.

Pure semiconductors have a band gap of approximately $1\,\mathrm{eV}$ between the valence band and conduction band. By doping the semiconductor a new energy level is created inside the band gap. For an n-type semiconductor the new energy level of the donators is close to the conduction band, so a small energy of approximately $25\,\mathrm{meV}$ (e.g. thermal energy) is sufficient to excite electrons into the conduction band. For a p-type semiconductor the newly introduced energy level of the acceptors is close to the valence band, so excitation into the acceptor band creates holes in the valence bands, which account for the conductance. The Fermi energy level of an unbiased semiconductor lies between the donor and the conduction band for an n-type semiconductor and between the acceptor

and the valence band for a p-type semiconductor. When joining an n-type and p-type semiconductor to form a p-n-junction the Fermi energy level of the two semiconductors has to be the same, so the n-type semiconductor has a lower level of the valence and conduction band compared to the p-type semiconductor. This induces a concentration gradient of electrons and holes, which causes diffusion. This creates a depletion zone and an electric field, which opposes the diffusion process, so an equilibrium with a diffusion potential $\varphi_B \approx 0.7\,\mathrm{V}$ is reached. Figure 1.1 shows the bent valence and conduction bands as a consequence of a constant Fermi energy.

Such p-n junctions are used in most semiconductor devices such as diodes and transistors. The photodiode is probably the most simple semiconductor photodetector and the basis of more sophisticated semiconductor photodetectors. The basic photodiode consists of a p-n-junction with a large but thin depletion zone. When the depletion zone is struck by a photon of sufficient energy an electron is excited, thus creating an electron-hole pair. Due to the diffusion potential φ_B, the electron moves to the cathode and the hole to the anode and produces a photocurrent instead of recombining.

One characteristic property of photodiodes is the quantum efficiency η. The quantum efficiency is the ratio between the number of generated electron-hole pairs, which reach the anode and cathode without recombining, and the number of incoming photons, which hit the depletion zone.

The *p-i-n* photodiode is a widely used special case of the *p-n* photodiode. It has a lightly doped intrinsic semiconductor between the p- and n-doped area, so there is a *p-i-n* junction. To optimize the quantum efficiency and frequency response the width of the depletion region can be adjusted with the intrinsic layer.

Photodiodes can be used in different operation modes. In the photovoltaic mode the photodiode is operated with zero bias voltage to achieve low noise and maximum energy efficiency. A popular example for this kind of device is the photovoltaic solar cell, which
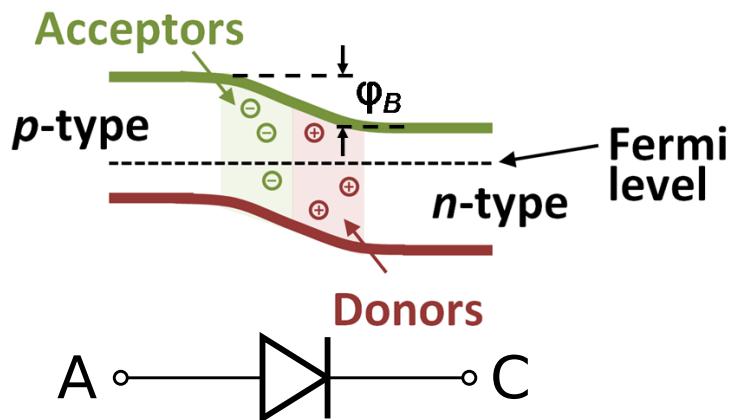

Figure 1.1: Band structure for p-n junction diode at zero bias. Original picture has been taken from [6], I have added the diode at the bottom.

is basically just a large-area p-n junction.

The photodiode can also be reverse biased to increase the width of the depletion zone, which decreases the capacity of the depletion zone. An increase of the depletion zone width results in a higher transit-time of the electron-hole pairs so a compromise has to be made to minimize the product of capacitance and transit-time for achieving a fast response speed. Such high bandwidth *p-i-n* photodiodes are ubiquitous in optical communication, which drives todays internet and information society.

A *p-i-n* was also used in the experimental setup to measure the light flux as explained in section 2.6.2.

All the described kinds of photodiode have a gain of 1 (i.e. no gain), therefore a high light flux and very sensitive electronic equipment is required for light detection. So for a measurement setup, which is sensitive to a few photons, an internal high gain of the photodetector is required. An internal gain can be activated by applying a high reverse bias voltage below the breakdown voltage of the diode. The resulting high electrical field accelerates the electrons and holes, which hit other electrons and holes and excite them to the conduction band, thus ionizing the semiconductor and creating new electron-hole pairs. The new electron-hole pairs are accelerated as well and increase the ionization rate, so the number of charge carriers increases exponentially. This process is called avalanche multiplication, hence such diodes are called avalanche photodiodes (APD). The noise increases rapidly with the overall multiplication factor M, thus the highest signal-to-noise ratio is reached by only $M \approx 10$ [1]. However, a gain of 100 to 1000 is possible by increasing the reverse bias voltage. Despite the internal gain of APDs, they still need to be hit by about 20 photons simultaneously for a detectable light pulse [3].

When the reverse bias voltage is increased beyond the breakdown voltage, the produced avalanche extends over the whole depletion layer, so the p-n junction becomes conducting. Thus, the diode current rises fast resulting in a high and fast signal. A quenching circuit is required, which reduces the bias voltage below the breakdown voltage shortly after the avalanche to quench the breakdown [7]. The operation mode above the breakdown voltage is called Geiger-mode in analogy to the Geiger-Müller counter, hence the avalanche photodiode becomes a Geiger-mode avalanche photodiode (G-APD) or single photon avalanche diode (SPAD). The amplitude of the generated signal depends mainly on the capacitance of the G-APD, as an avalanche discharges the G-APD. Thus every primary photoelectron is amplified by the whole charge of the G-APD, which results in a gain of 10^6 to 10^7 [8]. Like a Geiger counter, such devices are binary and can only give a signal whether one ore more photon has hit the diode. So for counting photons an array of G-APDs is needed, which leads us to silicon photomultipliers (SiPM) or multi-pixel photon counters (MPPC). The functionality and properties of silicon photomultipliers is the subject of the next section.

1.2. Silicon Photomultiplier (SiPM) Description

1.2.1. Topology

A silicon photomultiplier is a matrix of Geiger-mode avalanche photodiodes connected in parallel, which are the pixels of the SiPM. When a photon strikes a pixel it can trigger the Geiger discharge of the G-APD, which results in a current. The currents of the pixels add up, so the charge of the output signal is proportional to the number of simultaneously fired G-APDs which is proportional to the number of incoming photons for small light fluxes. For high luminosities the SiPM amplitude reaches a saturation, because each pixel can be fired only once until it is recharged [9].

The pixels consist of a n-type silicon substrate with an p-type layer above [7]. The typical depletion layer is very thin with about $0.7\,\mu$m, which produces the very high electric field of about $5 \cdot 10^5\,$V/cm for the Geiger discharge [10]. The pixels are connected in parallel with aluminium stripes to read out the combined pulse, which is the sum of all pixels. The pixels are electrically decoupled by polysilicon resistive stripes between the pixels.

Currently most SiPMs have a size of $1\,$mm $\times$ $1\,$mm and $3\,$mm $\times$ $3\,$mm and pixel sizes of $100\,\mu$m, $50\,\mu$m and $25\,\mu$m, which is also called the pitch of the SiPM. The actual active pixel size is smaller than the pitch due to trenches, quenching resistors and the Al contact grid between the pixels. The ratio between the active area and the square of the pitch is called the geometrical fill factor ϵ, which is typically between approximately $80\,\%$ down to $30\,\%$. Current SiPMs have between 100 and 14400 pixels [11].

1.2.2. Electrical Model

The SiPM is an electrical device, so an electrical model has to be developed to understand the behaviour and properties of SiPMs. Several electrical models with different elaborateness have been introduced and simulated so far [12, 13, 14].

The depletion zone introduces a capacitance to the pixel as it is basically a parallel-plate capacitor. The pixel can be regarded as a parallel circuit of a reverse biased diode and a capacitor with the pixel capacitance C_d. When the pixel is fired, the resulting avalanche makes the diode conducting so the capacitor is shorted and discharges.

The breakdown of the diode has to be quenched. Most of the time this is done passively with a quenching resistor. After the discharge of the pixel capacitance, the current starts flowing over the quenching resistor, which reduces the bias voltage U_{bi} at the diode below the breakdown voltage U_{br}. This stops the breakdown and the diode blocks the current again. The quenching resistor is made of polysilicon and has a quenching resistance in the order of $R_q \sim 100\,$kΩ. The quenching resistor also introduces a parasitic capacitance C_q. The quenching capacitance increases the pulse amplitude of the SiPM by introducing a spike component, since it is discharged during the breakdown of the pixel [13, 15].

All the pixels are connected to the bias voltage source over the bulk, which introduces the bulk resistance R_b. In addition the bulk introduces its own parasitic capacitance, the bulk capacitance C_b.

Figure 1.2 shows a schematic of the SiPM's electrical model.
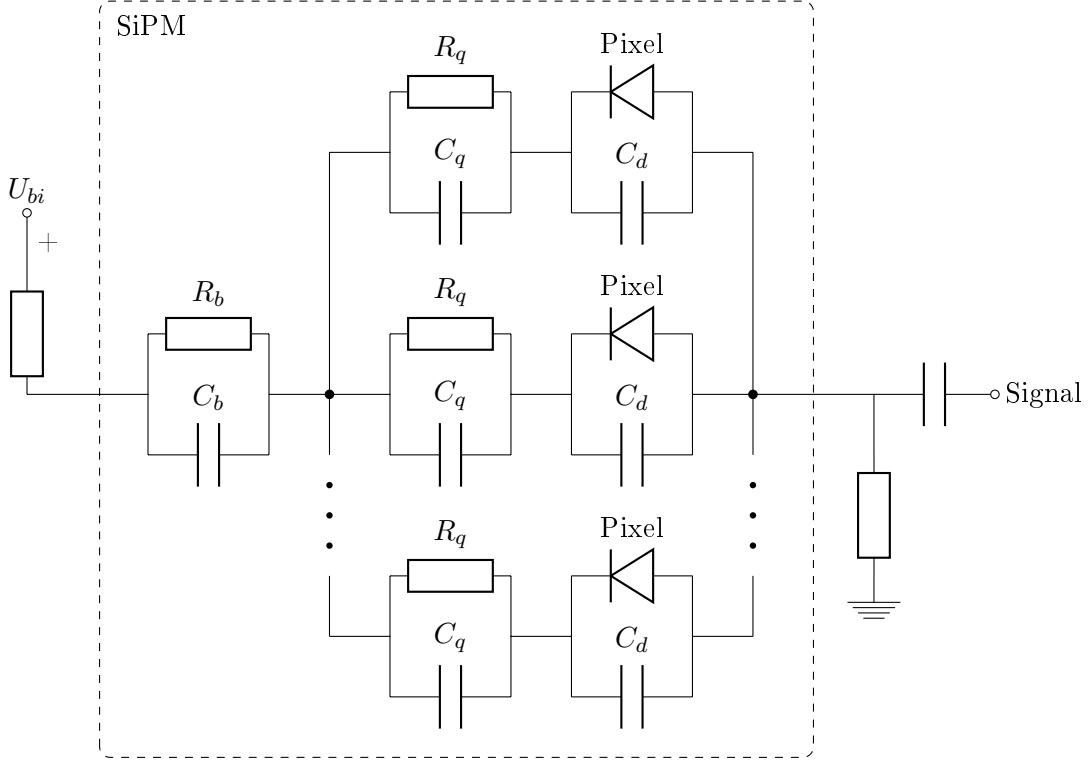
Figure 1.2: Schematics for the electrical model of the SiPM

After the breakdown of the pixel is quenched, the recharge of the pixel capacitance starts. The charging of a capacitor or rather of an RC circuit follows an exponential function:

$$U(t) = U_0 \left(1 - \exp\left(-\frac{t}{\tau} \right) \right) \quad \text{with } \tau = R \cdot C \tag{1.1}$$

Therefore, the smaller the resistance and the capacitance, the faster the capacitor is recharged. The parasitic quenching capacitance C_q is recharged nearly immediately, because R_b and C_q are much smaller than R_q and C_d [15]. The pixel capacitance C_d has to be recharged via the quenching resistor R_q. When the full SiPM is fired, the bulk capacitance is also discharged. This introduces a second and larger time constant to the recovery process, which is dominant in the tail of the recovery function of the SiPM.

Simulations of the electrical model of the SiPM have shown, that the pulse shape of the SiPM mostly depends on the electrical properties of the SiPM and not on the avalanche properties. These simulations have also confirmed the described electrical model, as they were able to reproduce the measured SiPM pulse shapes [16]. For instance adding the bulk capacitance C_b to the simulations introduced a second slow time constant in the tail of the pulses. Increasing the quenching capacitance C_q increased the pulse height but had only a very slight effect on the pulse shape.

Therefore, by studying the recovery time of the SiPM one can deduce electrical properties like the pixel capacitance.

1.2.3. Properties of SiPMs

1.2.3.1. Dark Noise

The noise of a photodetector in total darkness is called the dark noise. SiPMs have a relatively high dark noise rate of about $1\,\text{MHz}$ per mm^2 of active detector area at $25\,°\text{C}$. The dark noise events are triggered by thermally generated free charge carriers. The dark noise decreases by a factor of 2 for every $8\,\text{K}$ when the SiPM is cooled down [3].

The dark noise is distributed randomly, so the probability that several pixel fire simultaneously is very low, even when optical crosstalk is included (see section below). Therefore the dark noise is no issue if one sets a trigger threshold to events with several simultaneously firing pixels. However, this reduces the sensitivity of the SiPM, so it is not possible to detect single photons with SiPMs, because one can not distinguish between those single photon events, which were caused by an actual photon and those which were caused by a thermally generated electron.

1.2.3.2. Photo Detection Efficiency

The ratio of detected photons to incoming photons, which hit the detector area, is called the photo detection efficiency (PDE). The photo detection efficiency is the product of the quantum efficiency η, the geometrical fill factor ϵ and the probability that an electron-hole pair initiates a breakdown $P_{trigger}$ [3].

$$PDE = \eta \cdot \epsilon \cdot P_{trigger}$$

SiPMs typically have a PDE of 30% [17], which is competitive to photomultiplier tubes.

1.2.3.3. Afterpulsing

Afterpulses are caused by charge carriers, which are captured during the avalanche by deep level traps in the depletion area. After a statistically fluctuating delay these charge carriers are released and may trigger a new breakdown [7].

The probability of an afterpulse after a breakdown is typically about 20 % and increases with rising temperature and overvoltage [18].

Afterpulses increase the effective recovery time of the SiPM, as each afterpulse starts the recovery process anew.

1.2.3.4. Optical Crosstalk

Measuring the spectrum of dark noise events shows, that for approximately 10 % of events more than one pixel fires. This is significantly more than one would expect by random coincidence. The explanation for this excess is optical crosstalk.

As photons may create electron-hole pairs, the recombination of electron-hole pairs may also create photons. Hence, every avalanche may create a number of photons which in turn can trigger avalanches in the neighbouring cells. The probability that this occurs is called crosstalk probability, which is approximately the aforementioned 10 %.

1.2.4. Advantages and resulting possible Applications

The obvious contender of SiPMs is the well-established photomultiplier tube. The crucial property of photo detection efficiency is comparable with 30 % for both PMTs and SiPMs, although there are promising hints, that a higher PDE may be possible with SiPMs. One disadvantage of SiPMs is the much higher dark noise as compared to PMTs and the correlated noise as optical crosstalk and afterpulsing.

So in direct comparison PMTs may still seem like the better alternative at ideal conditions. Nevertheless, SiPMs have a few unique advantages over PMTs.

- Unaffected by magnetic fields: Large detectors at particle accelerators always use a strong magnetic field and the operation of photomultipliers in a magnetic field is problematic.

- Compact: Space is very much limited in most particle detectors and PMTs are much larger.

- Relatively low complexity and thus cheap: In contrast PMTs are handmade and require a vacuum inside.

- Very good timing resolution of about 30 ps.

- Relatively low operation voltage of 30 V to 70 V compared to $\mathcal{O}(\text{kV})$ of PMTs.

The first application of SiPMs which comes to mind are the places were PMTs are not usable due to a strong magnetic field and severe spatial constrains, which are particle detectors at accelerators as for example the CMS detector at the LHC. CMS currently uses APDs for its electromagnetic calorimeter. The disadvantage of APDs is, that they have a threshold sensitivity of 10 to 20 photons, so triggering on faint signals as minimum ionizing particles (MIP) is difficult. Thus the perspective to build a new CMS muon trigger with SiPMs for the sLHC upgrade is currently evaluated.

When upgrading the LHC for higher luminosities it is planned to possibly decrease the bunch spacing intervals down to 12.5 ns. For a high trigger efficiency it is crucial that the dead time of the trigger is shorter than the time to the next event. Therefore, a profound understanding of the recovery time of the used SiPMs is required to verify if SiPMs are fast enough for that purpose. An exact model of the recovery process of the SiPM could help to enhance the accuracy of the SiPM's measurements, since effects of the recovery processed as a reduced pulse height could be corrected in dependance of the time elapsed since the last event. A thorough calibration of the SiPM has to regard the influence of the previous events on the measured pulse. The first step to achieve that, is

the determination of a simple model for the recovery process of the SiPM including the recovery time as a parameter of the model.

The very good time resolution of SiPMs makes it a viable photodetector for positron emission tomography (PET) or for time-of-flight spectrometers. For instance the nuclear medicine group of our partner institute uses SiPMs for a time of flight spectrometer to determine the cross section of proton and carbon scattering [19].

A group at our institute is developing a prototype fluorescence telescope which uses SiPMs for the detection of cosmic-ray-induced air showers at the Pierre Auger Observatory. This also requires an as short as possible recovery time, because a shower evolves over a longer period of time during which the SiPM must not be saturated [20].

2. Experimental Setup

2.1. Idea

The recovery time of the SiPM is measured by first blinding it with a light pulse and then, after a variable time delay, flashing it with an identical probing light pulse. By measuring and comparing the two SiPM pulses in dependance of the relative time difference between light pulses the recovery process of the SiPM is investigated.

Figure 2.1 shows a block diagram of the experimental setup.
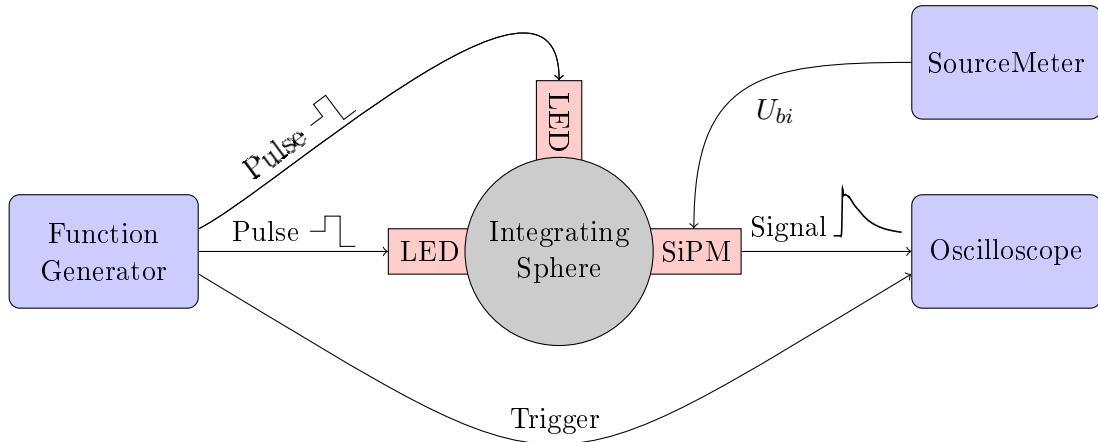
Figure 2.1: Block diagram of the experimental setup

An arbitrary function generator produces the two pulses with a variable time difference Δt. The light sources are LEDs, which have the advantage of being cheap and easy to handle. The LEDs and the SiPM are attached to an integrating sphere, which distributes the light diffusely.

An oscilloscope measures the two SiPM pulses, which are compared for varying time differences Δt.

9

2.2. Setup Description

I investigated the *S10362* SiPMs which are developed by HAMAMATSU [33]. Measurements were done for SiPMs with a size of $1\,\text{mm} \times 1\,\text{mm}$ and $3\,\text{mm} \times 3\,\text{mm}$ with pitches of $25\,\mu\text{m}$, $50\,\mu\text{m}$ and $100\,\mu\text{m}$. I had two SiPMs of each type and therefore 12 SiPM in total. Each available SiPM was studied to compare the results and to get a systematic characterization of all SiPMs.

Additionally a $3\,\text{mm} \times 3\,\text{mm}$ SiPM with $50\,\mu\text{m}$ pitch and 3600 pixels made by KETEK [34] is researched to get a comparison with a different type of SiPM.

To identify the SiPMs I use an identifier of the form *Area, Pitch, Serial Number*. So "$3 \times 3\,\text{mm}^2$, $50\,\mu\text{m}$, 2888" would refer to an SiPM with an active area of $3\,\text{mm} \times 3\,\text{mm}$ and a pitch of $50\,\mu\text{m}$ with a serial number of 2888. Such an SiPM would have $n = {}^{3^2\,\text{mm}^2}/_{50^2\,\mu\text{m}^2} = 3600$ pixels.

If not mentioned otherwise, I operate the SiPMs at the recommended bias voltage, which equates to a overvoltage ΔV of $1.9\,\text{V}$ to $2.5\,\text{V}$ depending on the SiPM.

The used LEDs have a wavelength of $(465 \pm 10)\,\text{nm}$ and are manufactured by THORLABS [35]. At this wavelength the photo detection efficiency (PDE) of the analyzed SiPMs reaches its maximum, so it is easier to blind the SiPM.

The LEDs are mounted inside 1" ($2.54\,\text{cm}$) lens tubes with matching LED mounts. The circuit board with one serial resistor (see section 2.6) is also put inside the lens tube. The lens tube is sealed with an end cap, in which a hole for a LEMO plug is milled.

For producing diffuse light with both LEDs I used an integrating sphere. This is a sphere with a diffuse reflective inner surface and four ports. The light enters at one port and is diffusely reflected until it hits any port. I attached the two LEDs at the opposing ports and mounted the SiPM to the upper port. The spare port can be used for an additional light sensor which can measure and monitor the light flux inside the integrating sphere (see section 2.6.2). The used integrating sphere *IS200-4* is made by THORLABS [36]. It has a diameter of 2" ($5.08\,\text{cm}$) and has a reflectivity of approx. 99% for most wavelengths. The ports of the integrating sphere have a diameter of 0.5" ($1.27\,\text{cm}$), so a 0.5"-to-1" adapter is used to attach the LED tubes and the SiPM to the integrating sphere. The SiPM mounts for the two SiPM sizes were made by the workshop of our institute and have a diameter of 1" to be compatible with the lens tubes.

As a light sensor the calibrated *p-i-n* photodiode *S9195* by HAMAMATSU [37] is used, which has an active area of $5\,\text{mm} \times 5\,\text{mm}$. (See sections 2.6.2 and 2.7 for more details.)

The pulses are generated by the *AFG3252* arbitrary function generator by TEKTRONIX [38], which allows full control over the pulse shape and the time difference between the pulses. The AFG is programmed via USB using the USBTMC Linux kernel driver. (See section 2.3 for more details.)

As a voltage source for the bias voltage of the SiPM the SourceMeter 2400 by KEITHLEY [39] is used. As this device provides also high precision measurements of the supplied current, it is used for the measurement of the characteristic U-I curves of the LED and the SiPMs as well. (Compare section 2.6 and 2.8.)

For the measurements with the *p-i-n* photodiode, which require an even higher precision of the measured electric current, the Picoammeter 6485 by KEITHLEY [40] is used.

The SiPM pulses are measured by the LECROY WavePro 725Zi oscilloscope [41] which can do online pulse analysis as for example determining the pulse height or the peak-to-peak amplitude. The communication with the oscilloscope is done over TCP/IP with the proprietary VICP[1] protocol. (See section 2.3 for more details.)

Figure 2.2 shows a photo of the experimental setup including the used devices.

Ideally I would have done the measurements in a temperature controlled environment, because nearly all properties of SiPMs show a strong temperature dependance, which is characteristic for any semiconductor device. Unfortunately this was not possible in our laboratory, so there is a systematic effect of the temperature in all measurements. All measurements were done at a temperature between $22\,^\circ$C and $30\,^\circ$C.
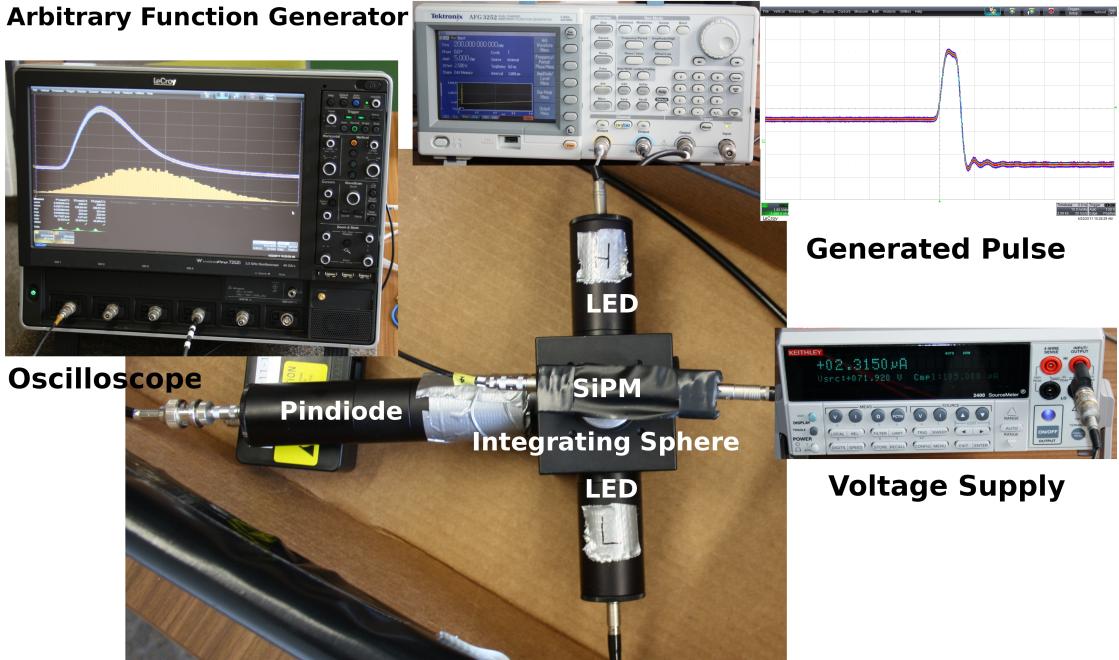
Figure 2.2: The experimental setup including the used devices

2.3. Data Acquisition

2.3.1. Communication with the Devices

The WavePro 725Zi oscilloscope provides an Ethernet interface for remote control. The communication uses the proprietary VICP protocol by LECROY, which is implemented on top of TCP/IP. I implemented the VICP protocol as a new module in *LibLAB*.

---

[1]VINES[2] Internet Control Protocol
[2]Virtual Integrated NEtwork Service

LibLAB is a laboratory software framework which is developed at our institute with the purpose of collecting source code for the control and operation of laboratory devices. It provides a similar API for different devices and encourages code reuse for related devices. Following this philosophy the implementation of the VICP module allows using it with any device which supports the VICP protocol.

Unfortunately the WavePro 725Zi provides only a very limited set of commands for remote control. For more sophisticated features of the oscilloscope one has to use the provided Visual Basic API on the device. Fortunately there is a remote control command for sending Visual Basic code to the oscilloscope, which is then executed on the device. In this way there is granular access to the state of the device in an object-oriented manner.

The AFG3252 function generator is controlled over the USB Test and Measurement Class (USBTMC) interface. The USBTMC standard specifies the communication with measurement devices via USB, so the communication with any device which implements the USBTMC specification can be done with the same driver. Here the USBTMC Linux kernel driver is used for communicating with the function generator. This driver provides a device under `/dev/usbtmc`, which can be read and written like any regular file.

2.3.2. Description of the Measurements

The measurement starts with setting up the arbitrary function generator. The function generator is set to burst mode with a trigger interval of 1 ms, i.e. every 1 ms the programmed waveform is emitted and an external trigger is sent. Both output channels are programmed to emit the desired pulse shape, but they are set to a different trigger delay so that the second pulse comes delayed.

The measurement of the SiPM pulses by the oscilloscope is triggered externally by the arbitrary function generator to minimize trigger jitter. The pulses are analyzed in real time by the oscilloscope and the absolute pulse height, the peak-to-peak amplitude and the area under the pulse is measured and saved in a histogram.

Each iteration of the measurements starts with setting the trigger delay of the function generator's second output channel to change the time difference between the two pulses. This variation of the time difference is done with a cubic scale, so I get more data points for smaller time differences than for large time differences. I expect that the second pulse changes faster at small time differences, because I expect an exponential recovery of the SiPM. By default the measurement starts at $\Delta t = 1000$ ns and ends at $\Delta t = 5$ ns.

Then the oscilloscope collects statistics of the above described values for a configurable amount of time. For most measurements that time was set to two seconds, which results in approximately 200 analyzed pulses. With a pulse trigger rate of 1 kHz one would rather expect 2000 measured pulses, but apparently the oscilloscope has a dead time of about 10 ms.

The pulse measurements are done for both pulses, by changing the trigger delay of the oscilloscope to the time difference of the two pulses. After the measurements the mean, the standard deviation and the number of measurements of each measured value is read over Ethernet and written to a file together with the set time difference of the pulses. Additionally the histograms of the values are saved, so that I can verify the distribution

of an outlying data point later. This process is repeated until the two pulses become indistinguishable.

Beside the sweep of the time difference I also save a configurable amount of raw waveforms of the SiPM pulse for doing a more sophisticated pulse analysis later, as for example a fit to the tail.

This whole measurement can be repeated n times to accumulate more statistics and to obtain an empirical statistical error.

The oscilloscope allows to define gates for the online pulse analysis. These gates restrict the range in which the measurement is performed. Since I know where the pulse will be located and can set the trigger delay of the oscilloscope accordingly, I can define a gate in which the pulse maximum will be located. This prevents errors and allows a better measurement of the second pulse, when it moves into the tail of the first pulse and becomes nearly indistinguishable from the first pulse. Of course any pulse measurement method needs a different gate, i.e. the peak-to-peak measurement needs a gate which includes the start of the peak and the peak maximum, while the absolute pulse height measurement should just include the peak maximum.

As intended, the gates have an influence on the results of my measurements. Since the choice of the gates is ambiguous, this choice induces a systematic uncertainty to my measurements. To estimate this uncertainty I carry out multiple measurements with different gate setups. Later a separate analysis is done for each of the gate setups and the resulting values are compared to estimate the systematic effect of the gate setup.

2.4. Arbitrary Function Generator Performance

2.4.1. Bandwidth

As I want to produce as short pulses as possible, it is necessary to understand the bandwidth limit of the function generator. The bandwidth of a device or a circuit is usually defined as the frequency at which the attenuation of the signal reaches $3\,\mathrm{dB}$ for a harmonic signal.

For the measurement of the bandwidth I configured the function generator to output a sine signal with a given frequency. This signal is measured by the oscilloscope which determines the amplitude of the signal and saves it into a histogram. Then the frequency of the signal is increased and for each frequency the measured amplitude and its standard deviation is saved. The used oscilloscope has a very high bandwidth of $2.5\,\mathrm{GHz}$, so the effect of the oscilloscope's bandwidth on the measurement is negligible.

The frequency response of a system is usually visualized in a so called Bode plot as shown in figure 2.3. In this plot the logarithmic attenuation in dB is plotted against the frequency of the signal in a logarithmic scale.

The measured bandwidth is $(262.0 \pm 0.1)\,\mathrm{MHz}$. The error was determined by repeating the measurement five times and computing the statistical error on the mean. The manufacturer specifies the bandwidth of the function generator as $240\,\mathrm{MHz}$, so the measured value is a bit higher.

This measurement shows, that pulses with a width of approx $250\,\text{MHz}^{-1} = 4\,\text{ns}$ should be possible, if a steep edge is not necessary.

Bode Plot
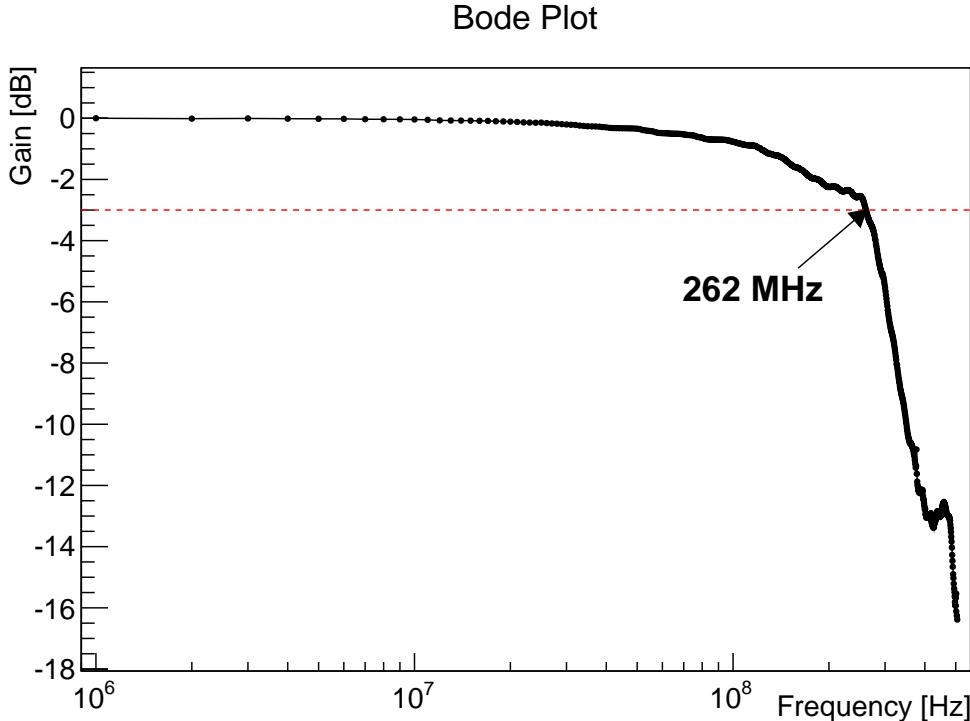
Figure 2.3: Bode diagram of the arbitrary function generator. The measured 3 dB bandwidth is $(262.0 \pm 0.1)\,\text{MHz}$, which is a bit higher than the specified bandwidth of 240 MHz.

2.4.2. Pulse Generation

As shown in section 2.4.1 the limited bandwidth of the function generator becomes an issue when generating nanosecond pulses. At a pulse width of approx. 5 ns the pulse height starts to drop dramatically. To increase the pulse height, I start the pulses at a baseline of $+1\,\text{V}$. Light measurements with a *p-i-n* photodiode (see section 2.7) showed, that at this voltage the LED does not yet emit light.

Figure 2.4 shows a plot of the pulse as it's saved in the arbitrary function generator. From the baseline of $+1\,\text{V}$ the voltage goes to $+4\,\text{V}$. The pulse width is 5 ns and after this time the voltage drops to $-1\,\text{V}$. These reverse bias voltage is used, to inhibit possible afterpulses of the LED. After that the voltage rises very slowly back to the baseline of $+1\,\text{V}$. This approach uses the function generator's maximal possible peak-to-peak voltage capability of 5 V.
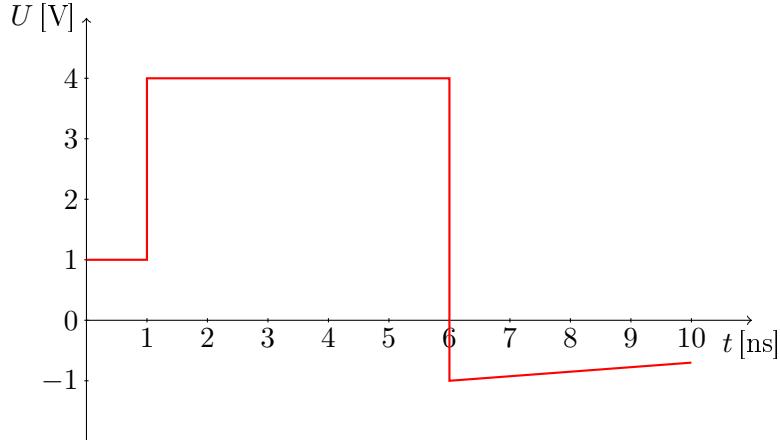
Figure 2.4: The pulse as it's set in the function generator

Figure 2.5 shows the actually created pulse of the function generator. The plot was created by measuring 500 waveforms of the output signal with the oscilloscope and filling these waveforms in a 2D histogram. The measured pulse differs from the set pulse in figure 2.4. It isn't a rectangular pulse with sharp edges but a rather smooth nearly sinusoidal pulse. This is expected due to the limited bandwidth of the function generator, as the rectangular pulse has high harmonics in its frequency spectrum. 4 V is also not quite reached because of the short pulse width.

Additionally there are oscillations after the edges. This shouldn't be an issue though, because these oscillations are mostly at the reverse bias voltage of $-1\,$V and should therefore not produce any light in the LED.

Altogether the generated pulses are sufficient for my measurements, although a shorter and higher pulse would be preferred.

2.4.3. Time Calibration

2.4.3.1. Measurement Description

Obviously for a precise measurement of the recovery time a profound understanding of the precision of the time difference between the blinding and probing pulses is required. This time difference is controlled by the function generator by changing the trigger delay of the second output channel as explained in section 2.3.2.

So a time calibration of the function generator was performed by measuring the time differences between the two pulses which are used for pulsing the LEDs. As a calibrated measurement device the oscilloscope is used, i.e. it is assumed that the time measurement of the oscilloscope is calibrated correctly.

For this measurement both output channels of the function generator are directly connected to the oscilloscope and the function generator is set up with the same configuration as described in section 2.3.2. The oscilloscope is configured to show both input channels
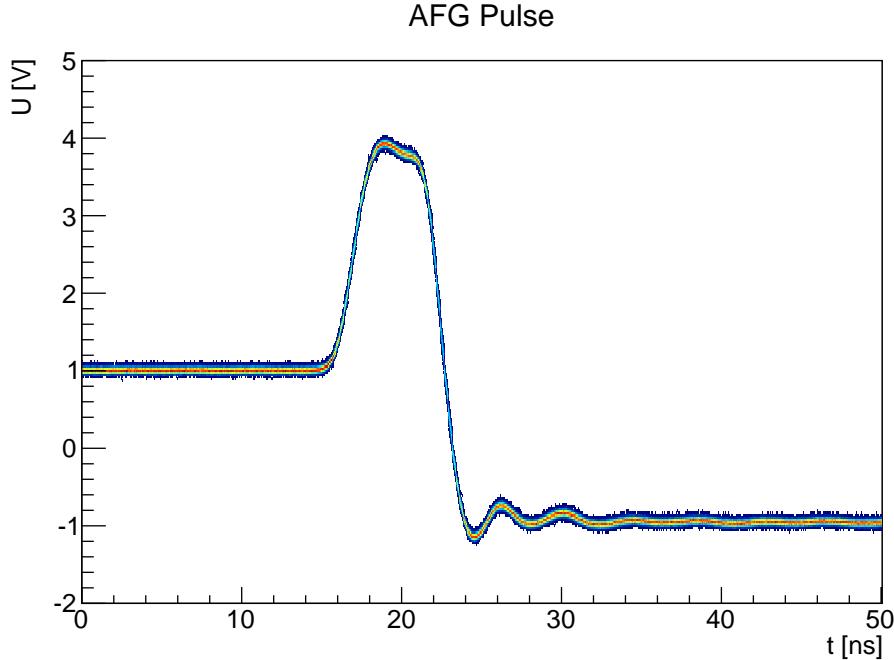
Figure 2.5: Overlay of measured waveforms of the generated pulse. The waveforms are plotted in a 2D histogram to imitate a persistence display to show the noise of the pulse. As you can see on the small line width of the waveform, the signal has a low noise, but there are stable oscillations after the edges. Due to the limited bandwidth of the function generator the generated signal isn't a rectangular pulse but has a more smooth and sinusoidal form.

and the time scale is chosen in such a way that it measures both pulses in one waveform. Then the time difference between the two pulses is measured and saved into a histogram. This measurement is done at two different heights in the edge of the pulse to compare the time stability of the pulses at different heights. The whole configuration resembles the features of a time to digital converter (TDC).

The sweep of the time difference between the pulses is done in the same way as described in section 2.3.2, with the only difference being that the time scale of the oscilloscope is changed to always measure both pulses no matter how big the time difference is.

2.4.3.2. Data Analysis

A first plot of the set time difference Δt of the AFG versus the measured time difference shows a very linear behaviour with a slope of virtually one. So to make any deviation from the linear function more visible figure 2.6 shows a plot of the difference between the measured Δt and the set Δt in dependance of Δt. Every data point is the mean of
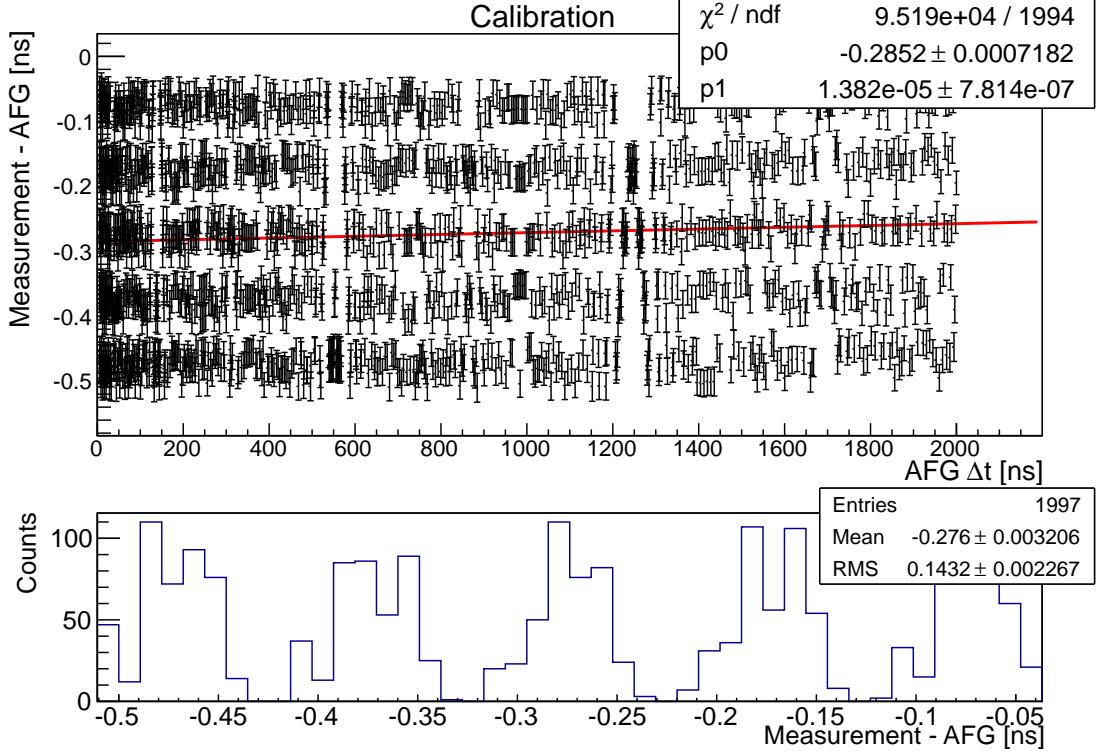
Figure 2.6: This plot shows the difference between the measured time difference Δt and the set time difference of the function generator in dependance of the time difference Δt of the pulses. Below that the histogram of the difference is shown, i.e. the projection of the data. In the histogram one can clearly see the discreteness of the time difference which shows the digital nature of the function generator. The mean difference between the measurement and the AFG time difference is (-0.276 ± 0.003) ns, which is small but significantly different from zero. Due to the digital resolution the set time difference of the function generator has an uncertainty of 0.14 ns, which is sufficiently accurate for my measurements.

about 180 measurements and the drawn errors are the statistical errors on the mean.

The plot shows that there is a significant systematic discrepancy between the set Δt of the function generator and the measured Δt. The mean of this difference is (-0.276 ± 0.003) ns so in later measurements with the function generator this difference will be subtracted from Δt to correct this error. The more important fact is, that the difference is virtually constant, although the fit shows a slope which is contradicting to zero but this slope is negligible and insignificant compared to the error due to digitization.

It is clearly visible, that the data points vary more than their statistical errors would allow for different Δt. But they do so in a discrete manner, which implies an uncertainty by digitization. One can set the trigger delay of the pulser with an accuracy of 0.1 ns,

but the real output signal only changes when the trigger delay is changed by $0.5\,\text{ns}$. This explains the 5 peaks which you can see in the histogram of the data. The measured standard deviation $\sigma = (0.143 \pm 0.002)\,\text{ns}$ of the data also fits extremely well the expected digitization error which is $\sigma_{dig} = \frac{0.5\,\text{ns}}{\sqrt{12}} \approx 0.144\,\text{ns}$. Therefore the error on Δt is $\sigma_{\Delta t} = 0.144\,\text{ns}$ which is accurate enough for my measurements.

This measurement was repeated a few times with the same results inside the error margins.

To determine the noise or rather the jitter of Δt the fixed time difference between two pulses was measured for a long time with 3.8 million measurements. Figure 2.7 shows the distribution of Δt with a fit of a gaussian. As you can see the histogram resembles extremely well a gaussian distribution with a standard deviation $\sigma = (0.0206 \pm 0.0001)\,\text{ns}$ which is negligible compared to the standard deviation due to the digitization of the function generator. Additionally the digitization of the oscilloscope is not visible which is not unexpected at a remarkably high sampling rate of $40\,\text{GS/s}$.

This measurement shows also that pulses of the function generator are very stable over a long period of time.
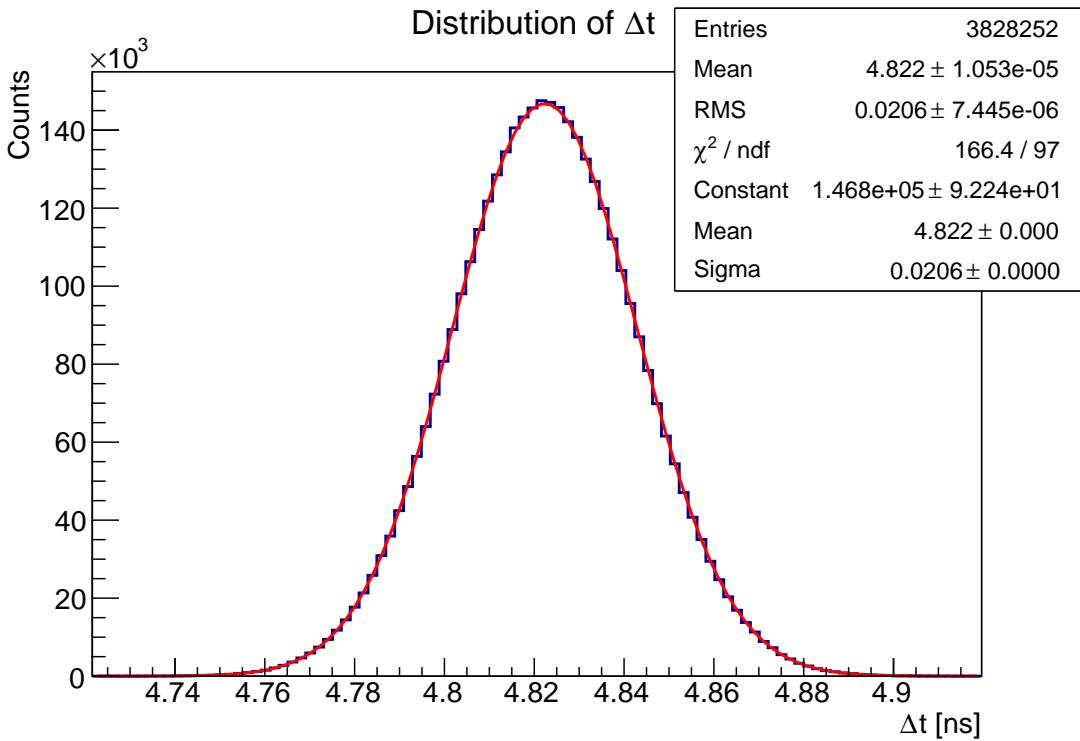

Figure 2.7: This histogram shows the distribution of the time difference Δt between two pulses as measured by the oscilloscope. As the fit shows, the data fits to a gaussian model even with very large statistics. The time difference is also stable over a long duration as the measurement lasted over an hour.

2.5. SiPM Readout

The SiPM is connected to the circuit described in figure 2.8. The applied bias voltage is filtered with a π-filter for getting a smooth DC signal without distortion from other power supplies at $50\,\mathrm{Hz}$. The circuit for getting only the AC signal of the SiPM by capacitative coupling is suggested by HAMAMATSU in their data sheets [11].
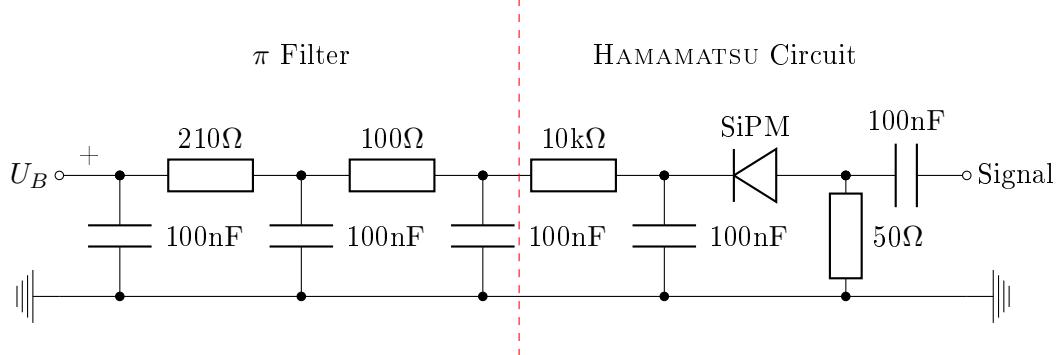
Figure 2.8: Schematic diagram of the circuit for operating the SiPM. The purpose of the π-filter is to filter distortions with about $50\,\mathrm{Hz}$ from the applied bias voltage from and the HAMAMATSU circuit provides the SiPM signal with capacitative coupling to only get the AC signal.

The cables for the bias voltage and the SiPM signal are connected with LEMO connectors, which are soldered to the circuit board. The whole circuit is wrapped in aluminium foil to provide electrical shielding against distortions.

No amplifier is used, because the blinded SiPMs provide pulse heights from $25\,\mathrm{mV}$ to $1000\,\mathrm{mV}$ depending on the SiPM size and number of pixels. This amplitude is sufficient for our oscilloscope which has an 8-bit resolution on a minimal range of $10\,\mathrm{mV}$. Without any amplifier there aren't any of the usual problems with shifting baselines or a low bandwidth of the amplifier. Measurements of the bandwidth of the used circuit showed a bandwidth of approximately $500\,\mathrm{MHz}$ [21], hence there isn't any systematic effect on the recovery time due to the used circuit.

2.6. LED Characteristics

2.6.1. Characteristic I-V Curve

For achieving nanosecond pulses, the LED circuit needs a high bandwidth and thus every electrical component needs to be terminated properly. Electrical termination means, that the impedance of our circuit is matched by a resistor to prevent interference of the pulses by signal reflection. As described by the Telegrapher's equations the signal reflections disappear if the impedance of the termination resistor is the same as the impedance of the circuit.

Unfortunately I didn't have the equipment to measure the complex impedance of our LED, so measuring the resistance of the LED for different applied voltages had to suffice. I made a sweep of the applied voltage and for each voltage the electric current was measured five times to get an estimate of the statistical errors by calculating the standard deviation of the measured values. This measurement was performed with the sourcemeter [39].

To get the resistance R of the LED in dependance of the applied voltage and current, $R = \frac{dU}{dI}$ is calculated by deriving the data numerically. Figure 2.9 shows the measured resistance in dependance of the applied voltage. The resistance shows an exponential behaviour, as one would expect for an LED. As you can see, $18\,\Omega$ is a realistic working point of the LED. As expected, the resistance of the second used LED shows the same characteristic curve.
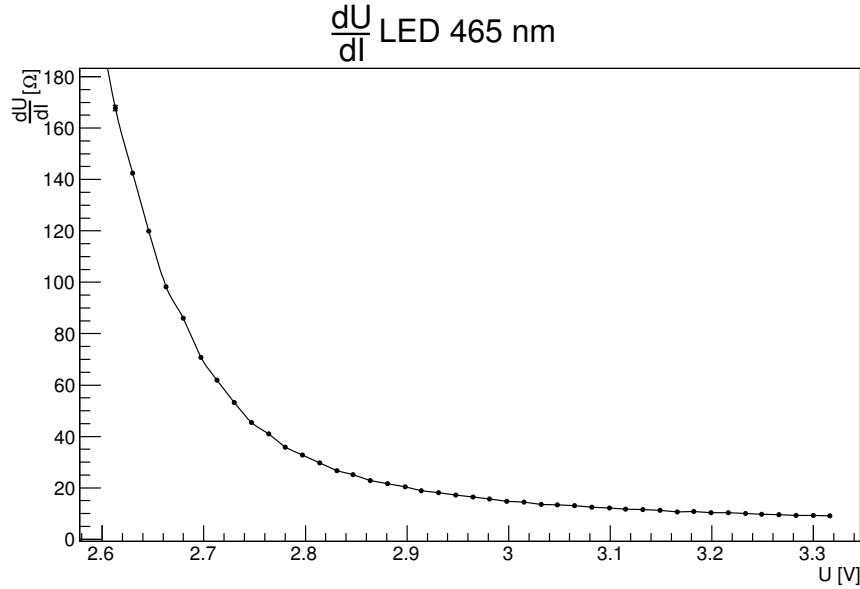

Figure 2.9: Resistance of the LED as function of the applied forward bias voltage. The resistance was calculated by numerical derivation of the characteristic I-V curve.

As a compromise of a minimal total resistance and an ideal terminator resistor I use a resistor with $R = 18\,\Omega$ as a passive terminator of the LED by connecting this resistor in series to the LED. The measured physical resistances of the used components are $(18.2 \pm 0.1)\,\Omega$ and $(18.1 \pm 0.1)\,\Omega$. This compromise provides both sufficient luminosity and prevents any signal reflections, as shown later in section 2.6.2.

These resistors are soldered on a circuit board with connectors for the LED and the signal. The circuit board is put inside the lens tubes and is connected to the signal plug in the end cap and to the LED in the LED mount on the other side. You can see a photo of the attached LED tube in figure 2.2.

2.6.2. Pulsing

2.6.2.1. Light Flux

To check if it is possible to blind the SiPM (i.e. to fire almost all pixels) with my setup, I measured the light flux inside the integrating sphere to determine the average number of photons per pulse and area.

To determine the light flux inside the integrating sphere a calibrated *p-i-n* photodiode is used. A *p-i-n* photodiode has a *p-i-n* junction instead of a *p-n* junction with a lightly doped intrinsic semiconductor between the p- and n-doped areas. When a photon hits the depletion zone an electron-hole pair is created with a probability in the order of 50%, which is called the quantum efficiency η. Thus the light-induced current is proportional to the light flux Φ with $I = 2\,\eta(\lambda) \cdot e \cdot \Phi$. The factor 2 takes into account, that a negative electron and a positive hole is created by the photon. For a more thorough description of semiconductor light detectors see section 1.1 in the introduction.

The *p-i-n* photodiode is operated without any reverse bias voltage and the current is measured by a picoammeter [40]. The circuit for the readout of the *p-i-n* photodiode includes a π-filter for filtering power-grid-induced noise at 50 Hz. The *p-i-n* photodiode and the circuit board is put inside 1" lens tube and is attached to the integrating sphere as shown in figure 2.2.

From the measured current I calculate the light flux by using the calibration data supplied at 465 nm, which is the wavelength of the used LEDs. The average number of photons per pulse and area is determined by dividing by the used pulse rate of 10 kHz and by dividing by the area of the photo diode, which is $25\,\text{mm}^2$.

Figure 2.10(a) shows the measured distribution of photons per pulse and area for the first LED.

The average number of photons per pulse and area is $\overline{n} = (34.6 \pm 1.7) \cdot 10^3\,\text{mm}^{-2}$ with a standard deviation of $\sigma = 49\,\text{mm}^{-2}$. The given error is the systematic error on the calibration of the photodiode as given by the manufacturer. The statistical error on the mean is negligible.

The SiPMs with a pitch of $25\,\mu\text{m}$ have the highest pixel density of $1600\,\text{mm}^{-2}$, which is more than one order of magnitude smaller than the photon density in the pulse. Therefore in most cases nearly all pixels should fire, so the SiPM is blinded by the pulse.

Figure 2.10(b) shows the light flux of the second LED, which is significantly lower,

than the light flux of the first LED with $\overline{n} = (29.4 \pm 1.5) \cdot 10^3 \, \text{mm}^{-2}$ photons per pulse. However, this is not unexpected, as the LEDs are manufactured with tolerances, so distinct LEDs may differ. This difference in the light flux is acceptable though, as both LEDs provide enough light to blind the SiPM.

A measurement with a pulse rate of $1 \, \text{kHz}$ yields the same number of photons per pulse, so the amount of photons per pulse is independent of the pulse rate.


(a) first LED   (b) second LED
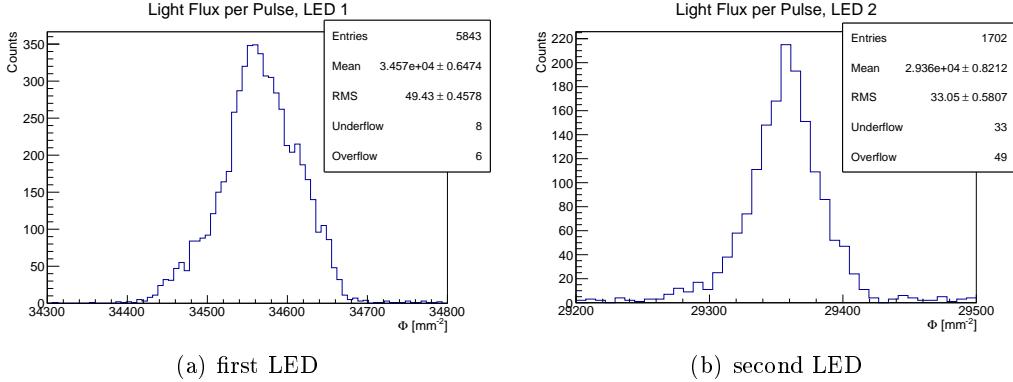
Figure 2.10: The distribution of the number of photons per pulse and area measured by a *p-i-n* photodiode. The mean light flux of the two LEDs differs significantly but both LEDs produce enough light for my purpose.

2.6.2.2. Coupling between LED and SiPM

When a small SiPM ($1 \, \text{mm} \times 1 \, \text{mm}$, $100 \, \mu\text{m}$ pitch) with a small output amplitude is used, large distortions of the SiPM pulse become visible. These oscillations in the pulse are stable for thousands of pulses, as you can see in the persistence display in figure 2.11, which implies that these distortions are not an effect of statistical noise but rather a systematic oscillation.

The reason for this distortion is the electrical coupling between the LEDs and the SiPM. Apparently the LEDs emit, besides the light, an electromagnetic wave at approximately $300 \, \text{MHz}$ which is picked up by the SiPM. Basically the LEDs and the SiPMs are antennas.

The above hypothesis was tested and proven by taping a patch of black felt in front of the SiPM, so that no light could hit the SiPM but the electromagnetic signal could still transit through the felt. The measured signal was just the above showed oscillations on the pulse without the actual pulse. As expected, I got the same signal, when I set the bias voltage of the SiPM to zero, so the pixels of the SiPM didn't fire anymore but the SiPM was still an antenna.

The solution for inhibiting the electrical coupling between the LEDs and the SiPM was to put the LEDs outside the dark box and to transport the light by an optical fiber. A fiber with a big diameter of $1 \, \text{mm}$ [42] was connected to the lens tubes of the LEDs

1x1 mm, 100 µm
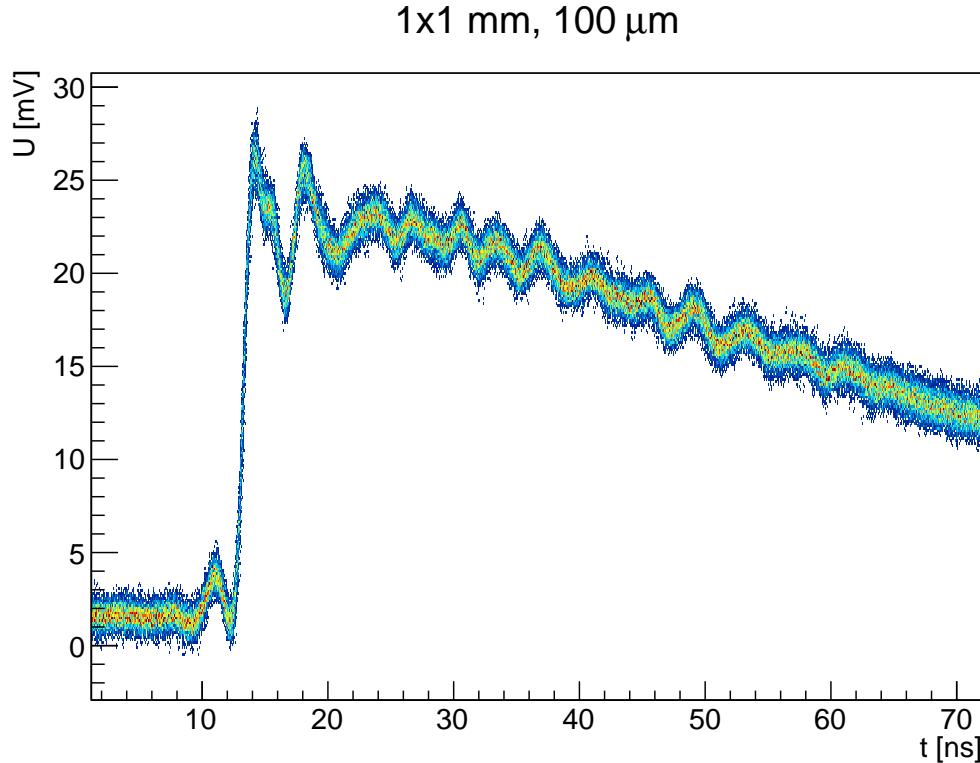
Figure 2.11: Waveform of a pulsed $1\,\text{mm} \times 1\,\text{mm}$, $100\,\mu\text{m}$ pitch SiPM. With low amplitude the oscillations due to electric coupling between the LED and the SiPM become visible.

and to the integrating sphere with compatible adapters. With this setup, the distortions disappeared as expected. Unfortunately the fiber reduces the light flux by a factor of 30 ± 1 as a measurement with the photodiode showed. This light flux isn't sufficient anymore to blind the big SiPMs with high pixel densities. However, the pulses are bright enough to blind the small SiPM, which also shows the largest distortions. Hence only a few measurements could be done using the fiber.

A number of measurements were done to compare the measurements of the recovery time with and without fiber to determine the effect of the distortions on the recovery time. These measurements showed, that the distortions do not affect the recovery of the SiPM. They only increase the difficulty of the data analysis a bit, as they induce systematic discrepancies to the expected exponential model. These measurements will be discussed more thoroughly later.

2.6.2.3. LED Pulse Shape

It is important, that there isn't any post-pulse oscillation in the light pulse, as these additional photons could fire pixels on the SiPM and thus disturb the SiPM's recovery process. This would lead to a systematic increase in the measured recovery time.

The first idea was to measure the pulse shape of the LED directly with the *p-i-n* photodiode and the oscilloscope. Unfortunately the oscilloscope is not sensitive enough to measure the tiny currents of the photodiode on such short timescales.

So the alternative idea was to measure the pulse shape of the light pulse with a SiPM using a filter to attenuate the light. The used filter absorbs 50% of the light. In addition the light is transmitted over a fiber, to minimize the electrical distortions in the pulse, as explained in section 2.6.2.2.

A $3\,\text{mm} \times 3\,\text{mm}$ SiPM with 3600 pixels is used. With the full light pulse the pulse height for this SiPM is $513\,\text{mV}$. After attenuating the light pulse with the fiber and the filter, the measured pulse height is $112\,\text{mV}$, so approximately 20% of the pixels of the SiPM are fired. If there is any afterpulsing or correlated noise due to the light pulse, the SiPM should still be sensitive enough to measure this.
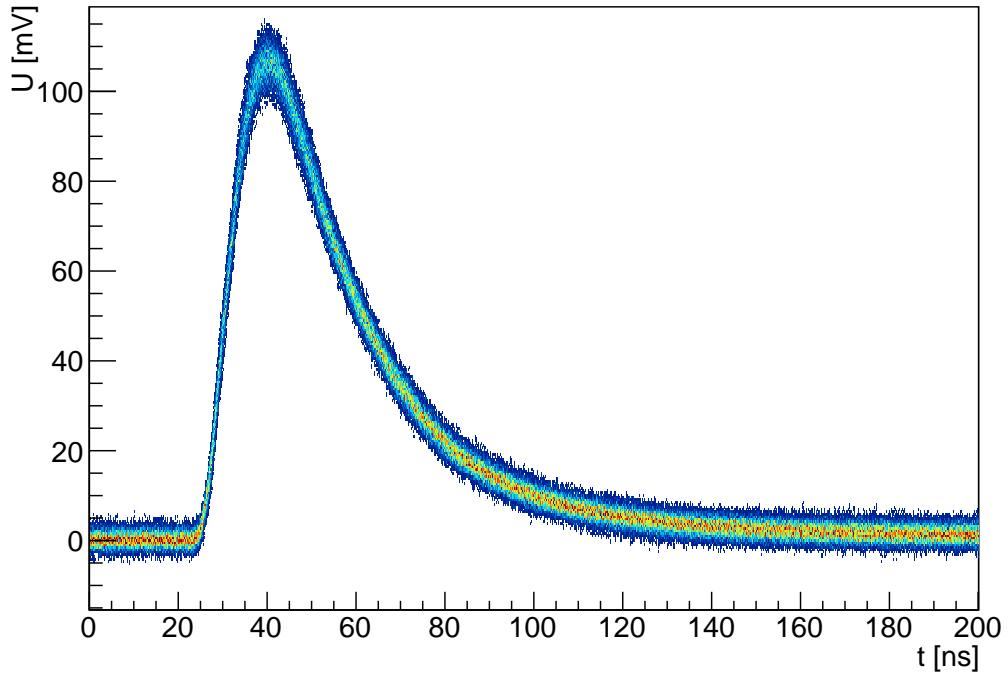

Figure 2.12: Attenuated light pulse measured with a $3\,\text{mm} \times 3\,\text{mm}$ SiPM with $50\,\mu\text{m}$ pitch. About 20% of the pixels fired. The smooth tail of the pulse shows, that there isn't any correlated afterpulsing or noise in the light pulse.

Figure 2.12 shows the measured SiPM pulse. The pulse shape is smooth and there aren't any oscillations or spikes as in figure 2.11. The random noise is relatively high, but this is mostly due to the lower signal and because the SiPM is sensitive to the random number of photons per pulse.

The conclusion from this measurement is, that the LED produces sharp light pulses without any post-pulse oscillations and the recovery of the SiPM is not disturbed by additional light. The distortions in figure 2.11 are only due to electrical coupling between SiPM and LED.

2.6.2.4. SiPM Saturation

Another question was, if the light pulse was really bright enough to fire all pixels of the SiPM, as estimated before. To test this, I attached the LEDs and the $3\,\mathrm{mm} \times 3\,\mathrm{mm}$ SiPM with $25\,\mathrm{\mu m}$ pitch directly to the integrating sphere. Then I slowly reduced the pulse height of the function generator while measuring the SiPM pulses with the oscilloscope.

The measured SiPM pulse height stayed virtually constant, until reducing the pulse height by approximately $200\,\mathrm{mV}$. When I further reduced the pulse height, the pulse height of the SiPM changed dramatically in an exponential manner.

The brightness of the LED changes approximately exponential with the applied voltage. Therefore this measurement shows, that virtually all pixels of the SiPM must fire, because reducing the amount of incoming light does not immediately change the pulse height, which is proportional to the number of fired pixels. Only after a specific threshold of light per pulse is reached, the SiPM pulse height starts to decrease with the incoming number of photons. Thus the SiPM is saturated and blinded by the light pulses.

2.7. Light-Tightness of the Setup

My experimental setup must be light-tight, because every photon which hits the SiPM during the recovery may cause an avalanche and thus extend the recovery process of the SiPM. As explained before, the SiPM has an intrinsic noise rate in the order of $1\,\mathrm{MHz\,mm^{-2}}$. The external noise rate due to randomly distributed photons should be well below this intrinsic noise rate, so that I can neglect the light noise.

The darkness is determined by measuring the light flux with the *p-i-n* photodiode as described in section 2.6.2. The light flux is measured with the two LEDs and the SiPM attached so the conditions are the same as in later measurements.

The calibration data for the *p-i-n* photodiode is wavelength dependant but the expected light noise is mostly caused by daylight, which has a very broad spectrum. To deduce the light flux from the measured current I assume that the wavelength distribution of the noise photons is uniform between 300 and 1000 nm and I calculate the mean of the calibration factors in that range. The range of light sensibility of the *p-i-n* photodiode matches that of the SiPM, so the wavelengths for which I will underestimate the light flux probably won't trigger the SiPM.

The distribution of the measured light flux is shown in figure 2.13(a). The measured mean is $\Phi = (75.6 \pm 5.0) \cdot 10^3\,\mathrm{s^{-1}\,mm^{-2}}$, which shows that light is leaking into the

(a) without dark box

(b) inside closed dark box
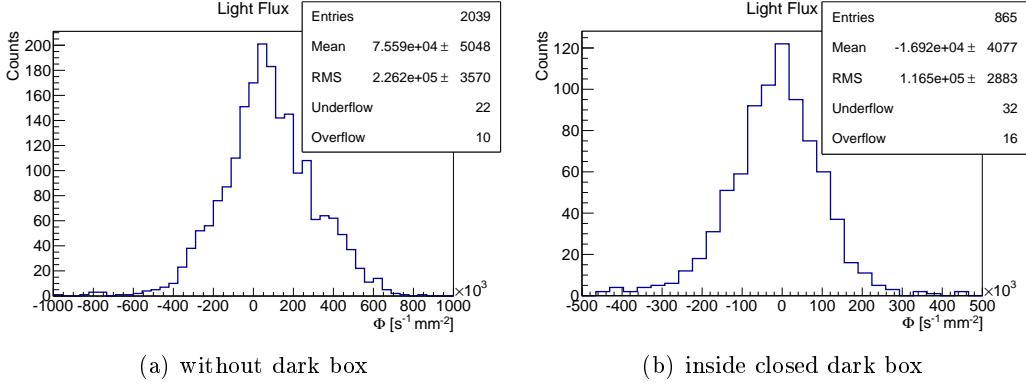
Figure 2.13: The distribution of the light flux in the integrating sphere measured by a *p-i-n* photodiode. The measurement was taken in daylight with ceiling lamps turned on.

integrating sphere. The light probably enters through the attached SiPM and LEDs. The measurement was taken in daylight with additional ceiling lamps turned on.

To increase the darkness of the experimental setup I put the whole setup in a cardboard box which was sealed against light with black felt. As figure 2.13(b) shows, the light flux drops below zero with a mean of $\Phi = (-16.9 \pm 4.1) \cdot 10^3\,\mathrm{s}^{-1}\,\mathrm{mm}^{-2}$, which shows that there must be a significant systematic offset in our measurement probably caused by a systematic error of the picoammeter.

(a) Opened dark box

(b) Closed dark box
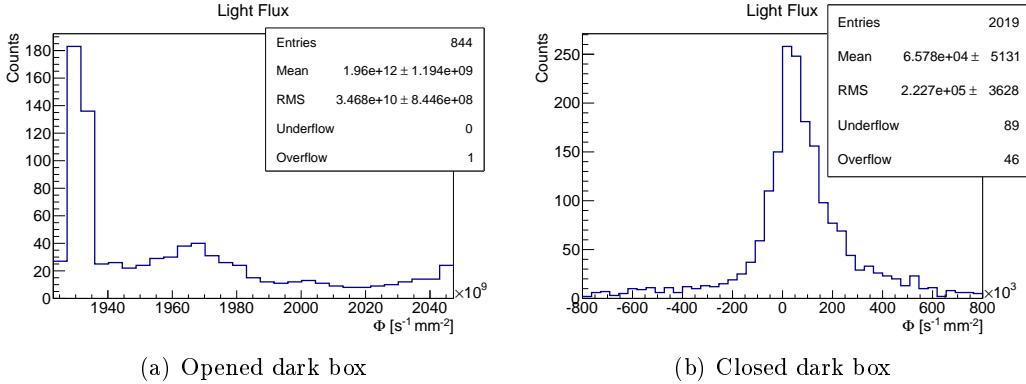
Figure 2.14: The distribution of the light flux in the dark box measured by a *p-i-n* photodiode. The measurement was taken in day light with the ceiling lamps turned on.

To get an estimate to what degree the dark box darkens the setup I put the exposed *p-i-n* photodiode without the integrating sphere into the dark box. Figure 2.14(a) shows the light flux while the dark box is open. As you can see in figure 2.14(b), the light flux

is reduced by a factor of $(30 \pm 2) \cdot 10^6$ when the dark box is closed.

So if I naively assume, that the darkening factor of the dark box and of the integrating sphere does not depend on the light flux, I get a rough estimate of $\Phi \approx 2.5 \cdot 10^{-3}\,\mathrm{s}^{-1}\,\mathrm{mm}^{-2}$. However naive that estimate may be, even if it would be off by a few orders of magnitude, my experimental setup would still be light-tight enough to neglect the influence of the light noise on the recovery of the SiPM. Therefore I assume that my experimental setup is light-tight.

2.8. SiPM Characteristics

As explained in section 1.2.2, to determine the capacitance of the SiPM's pixels from the recovery time the resistance R_q of the quenching resistor is required. In addition the breakdown voltage V_{br} is required to calculate the overvoltage ΔV from the applied bias voltage.

Both values can be acquired by measuring the characteristic I-V curves of the SiPM. R_q can be determined by measuring the resistance of the SiPM at high voltages when the resistance of the diode of the pixels vanishes. This happens at approx. $1\,\mathrm{V}$ in forward bias and at approx. $75\,\mathrm{V}$ in reverse bias. The breakdown voltage V_{br} is determined by measuring the voltage at which the current rises significantly.

The measurement of the characteristic curves is done with the sourcemeter [39] analog to the LED characterization described in section 2.6. The sweep of the voltage was done from approx. $-1\,\mathrm{V}$ to $75\,\mathrm{V}$.

Because the quenching resistors are made of polysilicon, the resistance strongly depends on the temperature. Additionally the breakdown voltage of semiconductor diodes also shows a strong dependance on the temperature. Thus the whole measurement was conducted in a temperature controlled environment at $(16.0 \pm 0.1)\,^\circ\mathrm{C}$.

For a proper characterization of the SiPM an actual measurement of the (complex) impedance would be required. For this one would need an AC voltage source with high voltages of up to $80\,\mathrm{V}$. Unfortunately such equipment is not available at our institute.

3. Data Analysis

3.1. Pulse Analysis

3.1.1. Introduction

Before a more thorough discussion of the systematic analysis of the SiPM pulses I want to discuss and visualize the most important features of the SiPM pulses, especially the probing pulse.

Figure 3.1 shows two close pulses of a completely fired $3 \times 3\,\mathrm{mm}^2$, $25\,\mathrm{\mu m}$ SiPM. The light pulses had a time difference of $\Delta t = 50\,\mathrm{ns}$ and the second pulse is on top of the tail of the first one.
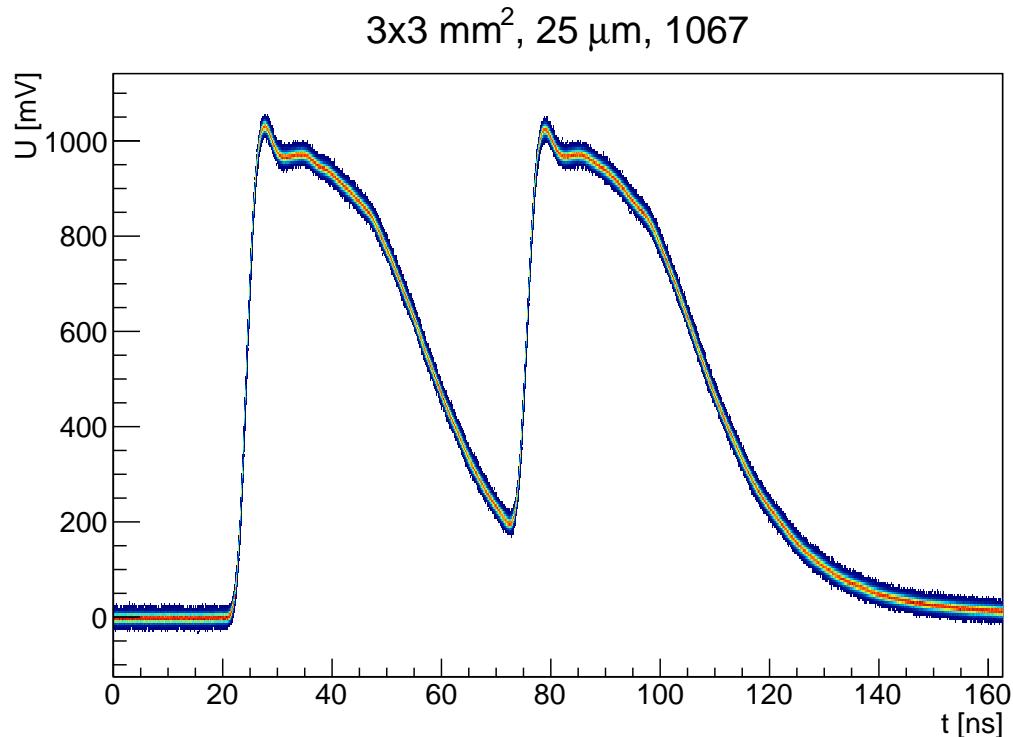

Figure 3.1: Two SiPM pulses with a time difference of $\Delta t = 50\,\mathrm{ns}$. The second pulse is as high as the first pulse, so the recovery time is mainly an effect of the tail of the first pulse, i.e. only the peak-to-tail amplitude decreases for small Δt.

The plot shows a few remarkable and to some extent surprising features of SiPM pulses. First of all, the absolute pulse height of the second pulse is about as high as the first pulse. The whole shape of the second pulse resembles the shape of the first pulse very much with the only difference, that the second pulse sits on top of the tail of the first pulse.

Thus, the only pulse parameter, which is significantly different for the second pulse, is the peak-to-peak pulse height or rather the "peak-to-tail" pulse height. The change in the peak-to-tail amplitude is nearly exclusively an effect of the tail of the first pulse, since the absolute pulse height of the second pulse stays constant. Therefore I concentrate my further analysis on the peak-to-tail amplitude and on the tail of the pulse itself.

The whole recovery process occurs on a timescale of a few tens of nanoseconds, which is surprisingly fast.

Another useful feature is the distinguishability of the two pulses. Even when reducing the time difference of the two pulses to $15\,\mathrm{ns}$, the second pulse stays distinguishable from the first pulse, so triggering on that pulse might still work.

This results are already surprising, as the literature so far reports recovery times in the order of microseconds [22, 23, 24, 3]. Additionally they report a decrease in the absolute pulse height after the SiPM is completely fired. They even define the recovery time with the decrease in pulse height of the probe pulse.

In contrast the pulse height of the KETEK SiPM [34] reduces significantly for small Δt as you can see in figure B.1. So the results in the literature could be explained by different or older SiPM types than the one I used [33].

3.1.2. Peak-to-Tail

As explained in section 2.3.2 the peak-to-peak amplitude of the two pulses is measured about 200 times for every time difference Δt. To analyze the recovery process I plot the ratio $\frac{A}{A_0}$ of the probing pulse amplitude A and the blinding pulse amplitude A_0 as a function of the time difference Δt as shown in figure 3.2.

One can clearly see the exponential drop in the amplitude for small Δt. However, fitting a single exponential function to the data shows, that the data actually differs significantly from the fitted function in the tail at large Δt. The data can better be described by a superposition of two exponential functions, with two different time constants:

$$f(\Delta t) = \frac{A}{A_0} - \exp\left(-\frac{\Delta t - t_1}{\tau_1}\right) - \exp\left(-\frac{\Delta t - t_2}{\tau_2}\right) \qquad (3.1)$$

There are five parameters in this model, namely τ_1, τ_2, t_1, t_2 and $\frac{A}{A_0}$.

As briefly described in section 1.2.2 τ is the recovery time of the SiPM, as it quantifies in which time the amplitude recovers to a certain level. I define τ_1 as the smaller time constant by initializing the fit with a small value of τ_1 and a larger value for τ_2. The dominating time constant τ_1 is the recovery time which corresponds to the recovery of the pixel capacitances C_d (see figure 1.2) and τ_2 is probably the recovery time of the bulk capacitance C_b. Simulations of the electrical model show, that the parasitic capacitance of the quenching resistor has only a negligible effect on the pulse shape [16], so the two
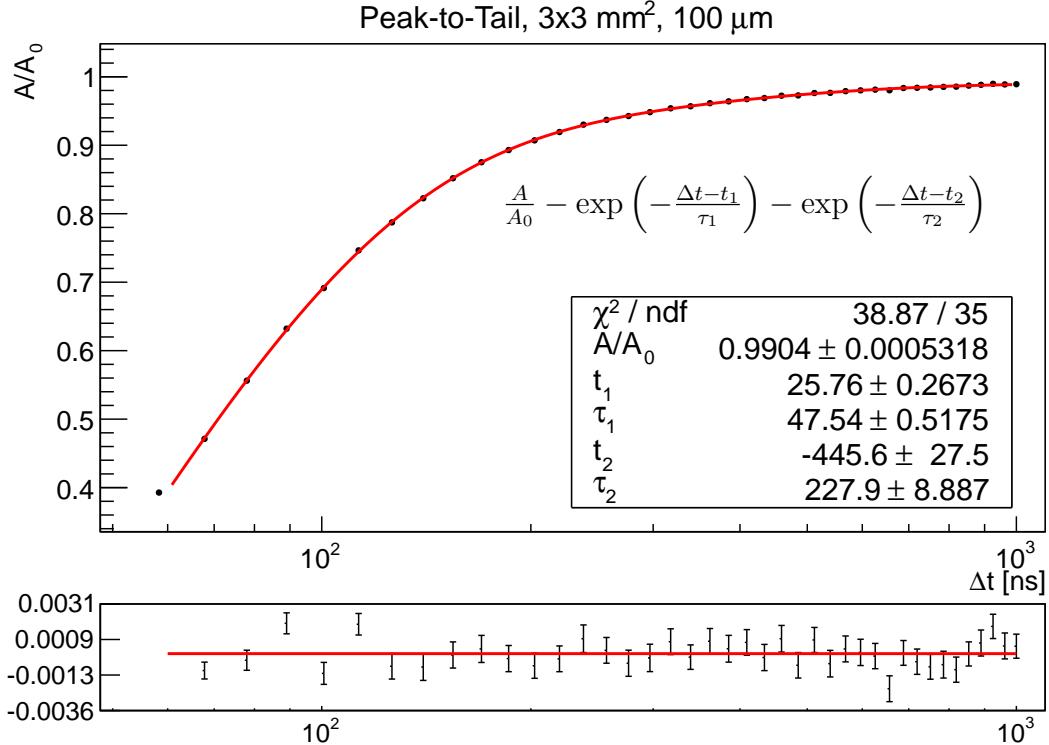
Figure 3.2: Peak-to-tail ratio of the blinding and probing pulse for the $3 \times 3\,\mathrm{mm}^2$, $100\,\mu\mathrm{m}$ SiPM. Every data point is the mean of about 200 pulses. The applied fit is the superposition of two exponential functions.

measured time constants probably correspond to the pixel capacitance C_d and the bulk capacitance C_b.

The time parameters t_1 and t_2 represent both the time delay and the amplitude of the exponential summand, because for exponential functions one cannot separate phase and amplitude, as they are the same. However, t_1 mostly accounts for the time after which the recovery of the SiPM starts.

The time constant t_2 acts more as an amplitude, as it is the reason that τ_2 is only dominant in the tail of the recovery, where the first summand is already converging. Hence the first summand with τ_1 is responsible for about 90 % of the SiPM's recharge. The smaller t_2, the smaller is the influence of the second term.

The parameter $\frac{A}{A_0}$ is the ratio of the peak-to-peak amplitudes when the SiPM is fully recovered. Ideally this would be 1, but as shown in section 2.6.2.1, the two LEDs don't emit the same light flux, so I expect a slight difference in pulse amplitudes of the SiPM. The discrepancy between this parameter and 1 is small (approximately 1 %), which is another proof that the SiPM is nearly completely fired.

For Δt smaller than 50 ns the data deviates too much from the exponential model,

because the second pulse moves into the shoulder of the first pulse. The SiPM pulse shape will be discussed in section 3.1.3.

Example plots of the peak-to-peak data with fit of every SiPM model are shown in the appendix in figure B.2 to B.8.

Almost every fit results in a $\chi^2/ndf > 1$, which shows that there are greater deviations from the fitted model as the statistical errors would allow. The residual plots show nearly the same systematic deviations for each measurement due to a systematic oscillation in the SiPM pulses. These distortions of the signal are an effect of the coupling between the LED and the SiPM, as explained in section 2.6.2.2. Because the distortions are mostly symmetrical, they should only have a slight effect on the fit results, as the fit averages them out.

I suspected that the errors on the fit parameters are underestimated due to the too large χ^2. To collect more empirical evidence of the statistical standard deviation of the fit parameters I repeated every measurement and the corresponding analysis 10 times. Then the weighted mean of each fit parameter is calculated and both the error of the weighted mean and the standard deviation of the 10 fit parameters are computed.

Table A.1 in the appendix shows the weighted mean and errors of all fit parameters. The fit parameters of measurements with the same configuration spread more than the statistical errors would allow i.e. there are a number of measurements which deviate by more than 5σ. However, on a short timescale the spread of different measurements is always within the expectation of the statistical deviation, as the mostly matching values in the columns σ^{stat} and σ^{fit} show. But when the measurement with the same configuration is repeated on the next day, I often observe recovery times which differ by several σ from the previously measured value. This is most probably due to changes in temperature, which varies on a larger timescale.

Section 3.4 shows an overvoltage dependance of the recovery time. The overvoltage strongly depends on the temperature, because the breakdown voltage itself is dependant on the temperature [25]. Hence, a temperature dependance of the recovery time is expected and further measurements in a temperature controlled environment are needed to quantify this dependance.

Therefore each result in table A.1 has to be regarded as a measurement at different conditions. The given recovery times are correct within their errors, but the exact conditions in which the SiPMs have this recovery times are unknown. Therefore I can only give a range for the recovery time of each SiPM type, as listed in table 3.1. Additionally the mean statistical error of the recovery time is given, so one can see that the range of determined recovery times spans over several σ.

As expected, the pixel recovery time τ_1 decreases with smaller pixel sizes, because the capacitance of the pixel decreases with the area. However, the area of the pixel changes by a factor of 4 between different SiPM types while the recovery time only decreases by a factor of approximately 1.8 to 2.5. Additionally the relative differences in the recovery time are larger for the $1 \times 1\,\mathrm{mm}^2$ SiPMs. Another surprise is the higher pixel recovery time of the $3 \times 3\,\mathrm{mm}^2$ SiPMs, as both SiPM sizes have the same pixel size. This implies, that either the quenching resistance R_q increases for smaller pixel sizes or the naive model of a simple capacitor does not correctly describe the pixel capacitance.

SiPM Type	τ_1 (ns) min $-$ max	$\overline{\sigma_{\tau_1}}$ (ns)	τ_2 (ns) min $-$ max	$\overline{\sigma_{\tau_2}}$ (ns)
$1 \times 1\,\mathrm{mm}^2$, $100\,\mathrm{\mu m}$	$37.5 - 44.7$	1.3	$115 - 203$	17
$1 \times 1\,\mathrm{mm}^2$, $50\,\mathrm{\mu m}$	$13.5 - 14.1$	0.1	$79 - 111$	8
$1 \times 1\,\mathrm{mm}^2$, $25\,\mathrm{\mu m}$	$7.6 - 8.8$	0.1	$41 - 144$	14
$3 \times 3\,\mathrm{mm}^2$, $100\,\mathrm{\mu m}$	$46.2 - 48.9$	0.1	$217 - 236$	3
$3 \times 3\,\mathrm{mm}^2$, $50\,\mathrm{\mu m}$	$19.1 - 19.8$	0.1	$96 - 129$	3
$3 \times 3\,\mathrm{mm}^2$, $25\,\mathrm{\mu m}$	$11.1 - 12.0$	0.1	$86 - 154$	21
KETEK 3×3, $50\,\mathrm{\mu m}$	$83.0 - 83.7$	0.1	$451 - 482$	15

Table 3.1: Summary of measured recovery times of different SiPM types. A range of recovery times is given, because the recovery time changes with the temperature. The given range is the recovery time for a temperature between $22\,\mathrm{^\circ C}$ and $30\,\mathrm{^\circ C}$. This table is the summary of table A.1 in the appendix.

The bulk recovery time τ_2 is a little larger for the $3 \times 3\,\mathrm{mm}^2$ SiPMs, but again not even close to an expected factor of 4.

It looks as if τ_2 decreases with smaller pixel sizes but the significance of the bulk recovery time τ_2 decreases also for smaller pixel sizes. For $50\,\mathrm{\mu m}$ and $25\,\mathrm{\mu m}$ pitches the actual effect of τ_2 on the tail of the recovery becomes too small, so the fit will sometimes result in a probably too low τ_2 with an also too small amplitude t_2. Therefore I can't make a statement if τ_2 really decreases with smaller pitches and the values for τ_2 shouldn't be trusted too much for small pixel sizes.

The larger statistical error on τ_1 for the $1 \times 1\,\mathrm{mm}^2$, $100\,\mathrm{\mu m}$ SiPM is probably due the lower pulse height of the SiPM, which makes the measurement more sensitive to distortions due to coupling.

Different SiPMs of the same SiPM type have the same recovery times within the systematic uncertainties due to the temperature fluctuations. This indicates, that the tolerances of the producer are probably below $10\,\%$, so different SiPMs of the same type have similar electrical properties.

As already mentioned in section 3.1.1 the KETEK SiPM [34] has a very different recovery process compared to the six different HAMAMATSU SiPMs [33]. The measured recovery times are both higher than any of the HAMAMATSU SiPM's recovery times despite the small pitch of $50\,\mathrm{\mu m}$. Additionally the large recovery time $\tau_2 \approx 460\,\mathrm{ns}$ is much more dominant, so it takes microseconds until the SiPM is fully charged again. This is more consistent with reports of the recovery time in literature [22, 23, 24] than the nanosecond recovery time of the HAMAMATSU SiPM.

3.1.2.1. Dependance of the Recovery Time on the Amplitude

To investigate a possible amplitude dependance of the recovery time I performed a number of measurements with different light pulse amplitudes. I started with an LED pulse amplitude of $3.0\,\mathrm{V}$ and increased the pulse height in steps of $0.1\,\mathrm{V}$ to the maximal peak-

to-peak capability of 5 V. For these measurements the fiber was used because at low amplitudes the distortions due to LED-SiPM-coupling became too dominant (see section 2.6.2.2). The LED pulses via fiber resulted in an SiPM pulse amplitude of 50 mV to 380 mV so 10% to 75% of the SiPM's pixels were fired.

Figure 3.3 shows the recovery time τ_1 in dependance of the SiPM pulse amplitude. Each fired pixel contributes to an increase in the pulse amplitude of about 530 mV/3600 ≈ 0.15 mV under the naive assumption, that the pulse amplitude increases linearly with the number of fired pixels. This relation is used to convert the measured pulse amplitude to the number of fired pixels in this section.

There is a rather linear increase in the recovery time with a slope of $m = (0.0025 \pm 0.0003)$ ns/pixel and the y-intercept is $n = (12.8 \pm 0.6)$ ns. The y-intercept is a rough estimate for the single-cell recovery time, but a more thorough research of single cell pulses is needed, because the slope might change drastically when only very few pixel fire. The single-cell recovery time could be determined by studying afterpulsing events and a single cell recovery time of approximately 9 ns has been reported for a 1×1 mm^2 SiPM with 50 µm pitch [26].

The increase of τ_1 could be explained by the coupling between the different pixels. If only a few pixels are fired, the charge of the not fired pixels could leak over the decoupling resistors of approximately 500 kΩ [27], thus recharging the fired pixels faster. If nearly all pixels are fired, the pixels have to be recharged by the voltage source and with charge from the bulk capacitance.

The bulk recovery time τ_2 is roughly constant as you can see in figure 3.4. There is a slight decrease in τ_2 though, but this is probably not significant.
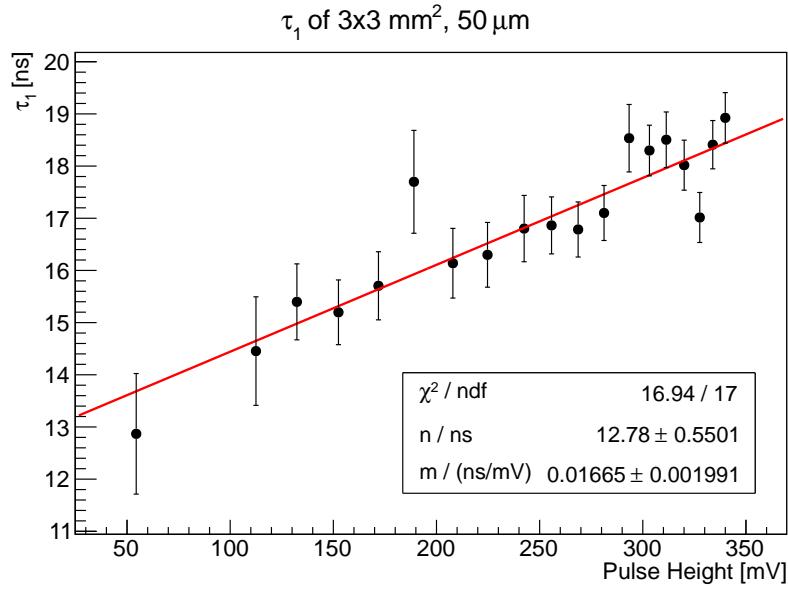
Figure 3.3: Recovery time τ_1 in dependance of the SiPM pulse height. The recovery time increases fairly linearly with the pulse height, i.e. the number of fired pixels with a slope of $m = (0.0025 \pm 0.0003)\,\mathrm{ns/pixel}$ and an y-intercept of $n = (12.8 \pm 0.6)\,\mathrm{ns}$.
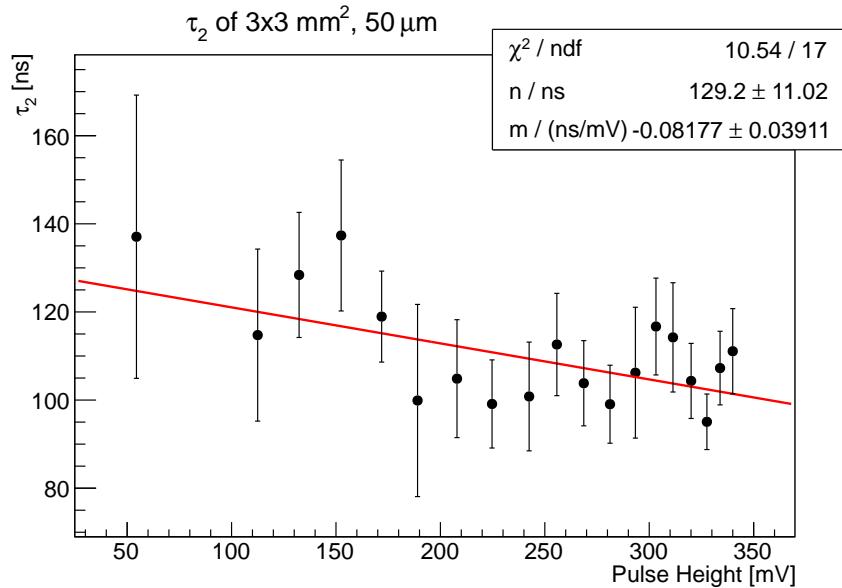

Figure 3.4: Bulk recovery time τ_2 in dependance of the SiPM pulse height, which shows that τ_2 is roughly constant.

3.1.3. Pulse Tail

The absolute pulse height of the probing SiPM pulse stays nearly constant, so the decrease of the peak-to-peak amplitude described in the previous section is mainly an effect of the pulse tail of the first blinding pulse. Hence, an analysis of the SiPM pulse tail should result in the same time constants as the analysis of the peak-to-peak measurements. The determination of the recovery time from the pulse tails has the advantage of a much simpler experimental setup, since only a single blinding light source would be required. In addition, the measurement can be performed very fast, because only the measurement of a number of SiPM pulses, without a sweep of the time difference Δt between two pulses, is required. Such a measurement could be performed in under $1\,\mathrm{ms}$ inside a detector to recalibrate the SiPM if the bandwidth of the front-end electronics is sufficient high.

To reduce statistical noise the mean of 200 measured waveforms is calculated for each data point in the waveform. The superposition of the two exponential functions as written in formula 3.1 is fitted to the tail of this average pulse. The used errors are the calculated errors on the mean.
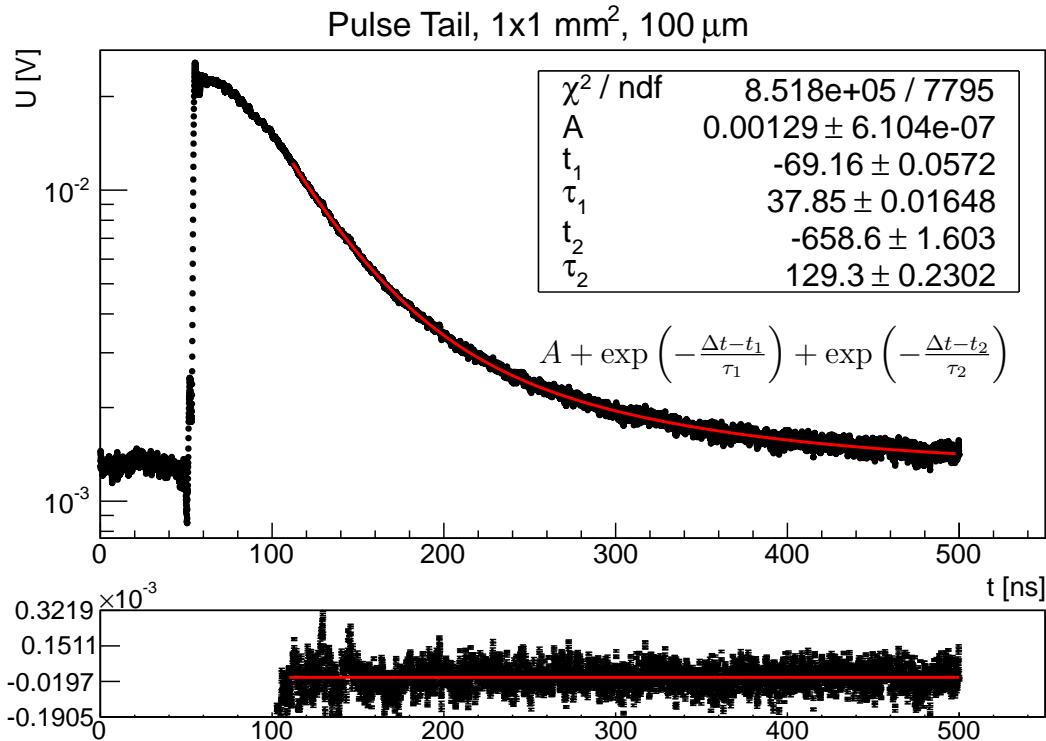

Figure 3.5: Average of 200 SiPM pulses with a fit of the pulse tail. The χ^2/ndf of the fit is too large due to the systematic oscillations on top of the pulse, which are much larger than the statistical noise.

As an example the fit of the pulse tail of the $1 \times 1\,\mathrm{mm}^2$, $100\,\mathrm{\mu m}$ SiPM is shown in

figure 3.5. Example fits for the other SiPMs are shown in figure B.10 to B.15 in the appendix. All pulses are modulated by an oscillation, due to coupling between the SiPM and the LED (see section 2.6.2.2). This leads to a much too large χ^2/ndf, because these distortions are systematic and stable for the duration of the measurement, so the statistic errors on the data do not account for these distortions. The bottom plot of figure B.9 shows a zoomed plot of the residuals, on which the systematic oscillations can be clearly seen.

The errors on the fit parameters are underestimated due to the too large χ^2, so it is necessary to repeat the measurement and the analysis several times to determine statistical errors. Table A.2 in the appendix shows a collection of fit parameters for different SiPMs and different fit ranges. The given fit parameters are the mean of 10 different measurements and fits. The given statistical errors are the errors on the mean.

Unfortunately τ_2 could not be determined for $3 \times 3\,\mathrm{mm}^2$, $100\,\mathrm{\mu m}$ SiPM, because the measurement gate was too short, so the tail of the waveform was missing.

The choice of the fit range has a strong effect on the results of the fit. The fit range was chosen such that the deviations in the residual plot are minimal with a fit range as large as reasonable. However, this criterion isn't well-defined, so this introduces a systematic error on the fit parameters due to the choice of the fit range. In order to estimate this systematic error, the analysis was repeated with three different fit ranges. First a fit with a moderate and most reasonable fit range was performed. Then I made fits with the widest reasonable fit range and with the narrowest reasonable fit range. The actual most reasonable and correct fit range should lie somewhere between the narrow and the wide fit range.

The fit parameters in table A.2 show, that the "narrow" fit range systematically yields the smallest recovery times while the "wide" fit range yields the largest recovery times. The true recovery time should lie somewhere between these largest and smallest results. The result of the "moderate" fit is an estimate for the true value of the recovery time and the results of the "wide" and "narrow" fit give the systematic uncertainties.

These systematic uncertainties on the fit range outweigh the statistical uncertainties and even the fluctuation due to temperature changes (see section 3.1.2), as one can see in the first 12 rows of table A.2. Due to that I don't list all results of the analysis in table A.2, because this wouldn't provide any additional information.

Table 3.2 shows a summary of table A.2. The recovery time τ_1 is systematically smaller than the results of the peak-to-tail analysis in table 3.1. Most of the ranges don't overlap or barely overlap. So even if the "wide" fit range would be the true fit range, the recovery time would still be smaller most of the time.

One reason for this could be, that a wider fit range of about $50\,\mathrm{ns}$ to $1000\,\mathrm{ns}$ is used for the peak-to-tail analysis, while the "wide" fits on the pulse tail are done between about $60\,\mathrm{ns}$ and $200\,\mathrm{ns}$. The deviations from the model become too large for smaller t, so that the fit wouldn't converge anymore. So for small t the peak-to-peak amplitude differs from the pulse, at least partly due to a decreased absolute pulse height (see section 3.1.4).

The determination of the bulk recovery time τ_2 is rather inaccurate, because the signal-to-noise ratio gets low in the end of the pulse tail, where the bulk recovery time dominates. Nevertheless, the determined τ_2 roughly matches to the previously determined values,

SiPM Type	τ_1 (ns)	$\overline{\sigma_{\tau_1}}$ (ns)	τ_2 (ns)	$\overline{\sigma_{\tau_2}}$ (ns)
	min $-$ max		min $-$ max	
$1 \times 1\,\mathrm{mm}^2$, $100\,\mu\mathrm{m}$	$34.5 - 41.8$	0.4	$94 - 163$	9
$1 \times 1\,\mathrm{mm}^2$, $50\,\mu\mathrm{m}$	$11.0 - 13.2$	0.6	$42 - 142$	14
$1 \times 1\,\mathrm{mm}^2$, $25\,\mu\mathrm{m}$	$5.9 - 7.2$	0.2	$28 - 65$	3
$3 \times 3\,\mathrm{mm}^2$, $100\,\mu\mathrm{m}$	$43.1 - 50.3$	0.2		
$3 \times 3\,\mathrm{mm}^2$, $50\,\mu\mathrm{m}$	$17.6 - 18.9$	0.2	$61 - 128$	14
$3 \times 3\,\mathrm{mm}^2$, $25\,\mu\mathrm{m}$	$10.4 - 11.3$	0.1	$32 - 132$	12
KETEK 3×3, $50\,\mu\mathrm{m}$	$76.9 - 96.0$	0.4	$625 - 1159$	19

Table 3.2: Results of the pulse tail fit. The fit range is not well-defined, so fits with different ranges were made and the resulting range of parameters is given. The given statistical errors are the standard deviation of 10 measurements with the same configuration. This table is the summary of table A.2 in the appendix.

although the values again are systematically smaller than in the peak-to-tail analysis.

3.1.4. Absolute Pulse Height

To take a closer look on the change of pulse height ratio of the two SiPM pulses I do the same analysis as explained in section 3.1.2 for the measured absolute pulse heights of the SiPM pulses. As shown in figure 3.6 and B.16 to B.21 in the appendix, there is only a small decrease in the ratio of the pulse height. This has already been observed by looking at the raw SiPM pulses with the oscilloscope, as shown in section 3.1.1.

The biggest decrease in pulse height for the HAMAMATSU SiPMs is observed (approximately 10%) for the SiPMs with $100\,\mu\mathrm{m}$ pitch. The pulse height of the SiPMs with $50\,\mu\mathrm{m}$ pitch decreases only by about 5% and for the SiPMs with $25\,\mu\mathrm{m}$ pitch the pulse height stays constant for every Δt (see for instance figure B.18).

The KETEK SiPM is the only investigated SiPM whose pulse height drops heavily by about 50% (see figure B.22). A larger decrease can not be observed, because at this low pulse height the SiPM pulse becomes indistinguishable from the tail of the previous pulse.

Table A.3 shows all fit parameters of the analysis as described in section 3.1.2. For the SiPMs with $100\,\mu\mathrm{m}$ pitch the fits showed that there are two time constants, but for the $50\,\mu\mathrm{m}$ pitch only one time constant could be determined. Performing the fits is difficult and rather inaccurate for this data due to the weak decrease in pulse height, so the results are more a rough estimate to do a consistency check with the rest of the analysis.

The recovery time of the pulse height roughly matches the previous results, although the pulse height recovery time mostly is a little smaller. Only the KETEK SiPM has a significantly larger pulse height recovery time than peak-to-tail recovery time (approximately 15%).

Altogether this analysis confirms the previous results.
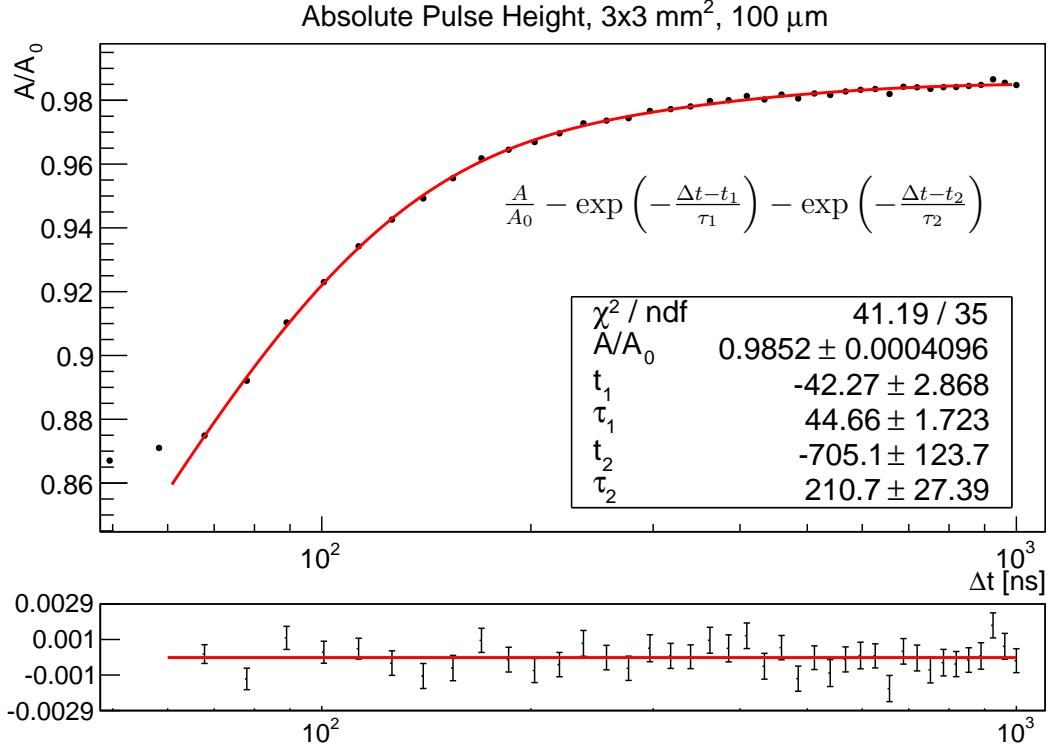
Figure 3.6: Amplitude ratio of the blinding and probing SiPM pulse. Every data point is the mean of about 200 pulses. The applied fit is the superposition of two exponential functions.

SiPM Type	τ_1 (ns) $\min - \max$	$\overline{\sigma_{\tau_1}}$ (ns)	τ_2 (ns) $\min - \max$	$\overline{\sigma_{\tau_2}}$ (ns)
$1 \times 1 \, \mathrm{mm}^2$, $100 \, \mu\mathrm{m}$	$37.8 - 55.4$	3.4	$101 - 112$	125
$1 \times 1 \, \mathrm{mm}^2$, $50 \, \mu\mathrm{m}$	$11.9 - 13.1$	0.3		
$3 \times 3 \, \mathrm{mm}^2$, $100 \, \mu\mathrm{m}$	$37.0 - 52.9$	0.6	$153 - 379$	21
$3 \times 3 \, \mathrm{mm}^2$, $50 \, \mu\mathrm{m}$	$15.6 - 18.8$	0.2		
KETEK 3×3, $50 \, \mu\mathrm{m}$	$95.2 - 95.5$	0.1		

Table 3.3: Summary of the fit parameters for the pulse height data. The pulse height drops only slightly for small Δt so this analysis is more a consistency check for the data in table 3.1

3.2. Characteristic Curves

The aim of this analysis is to determine the resistance of the quenching resistor R_q by analysing the measured characteristic I-V curves of the twelve used SiPMs.

Figure 3.7 shows logarithmic plots of the characteristic I-V curves of reverse biased SiPMs. Different SiPMs of the same model have nearly indistinguishable characteristic curves, so only one plot per SiPM type is shown in the figure.

The characteristic curves of all SiPMs show the same basic structure. At voltages below the breakdown voltage there is a small leakage current, which is around $0.1\,\text{nA}$. For the $1 \times 1\,\text{mm}$ SiPMs the leakage current is below the measurement sensibility of the picoammeter, so it isn't visible in the plot.

Then at the breakdown voltage the current increases exponentially by about two orders of magnitude. After that the current rises slower for about one order of magnitude. For smaller pixel sizes this plateau gets larger, i.e. more voltage is needed to reach the next regime with a higher slope. In the end the slope decreases again. In this regime at about $1\,\text{mA}$ the quenching resistors become the dominant resistance, so the determination of the quenching resistance is possible.
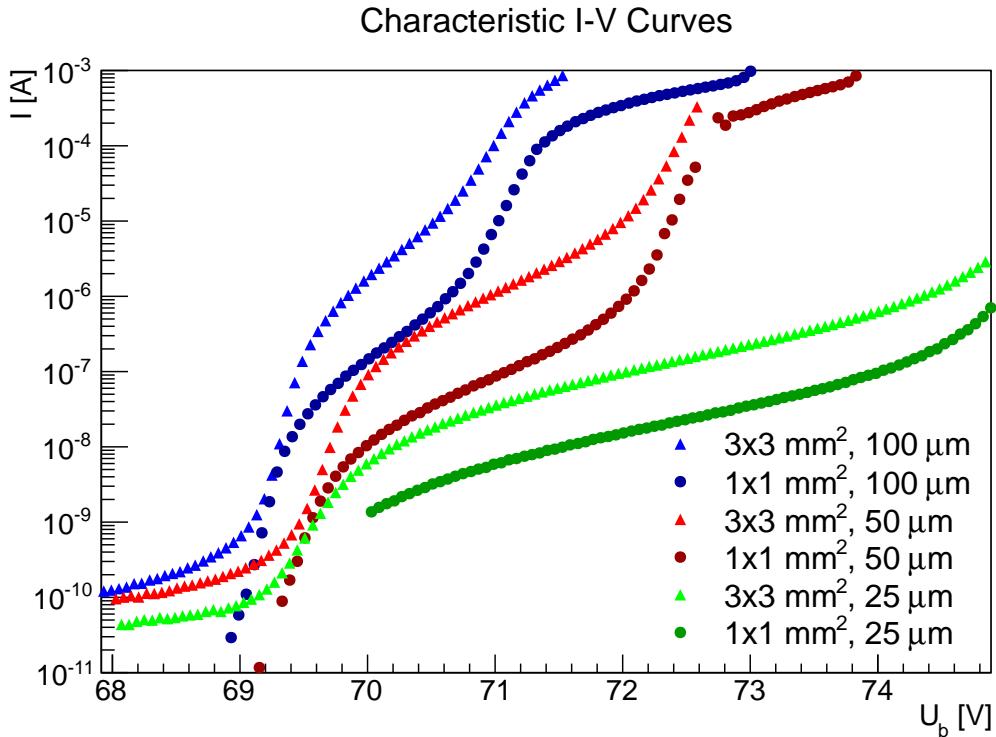


Figure 3.7: Characteristic I-V curves of different SiPM types

An avalanche model, which explains the shape of the characteristic I-V curve and the

systematics of the different SiPMs, has not yet been developed. This would be beyond the scope of this thesis, as I only want to determine the quenching resistance to calculate the capacitance from the recovery time.

The next measurement was done at a very high overvoltage to make sure, that the resistance of the diode is negligible compared to the quenching resistance. In this regime the current is expected to be proportional to the voltage, as implied by Ohm's law, so I can determine the resistance by doing a linear regression.

Figure 3.8 shows an example linear fit for the $3 \times 3\,\text{mm}^2$, $25\,\mu\text{m}$, 2888 SiPM. As you can see, the fit works well and the current is very linear.

Unfortunately, there are also measurements which show a more parabolic shape of the current, as you can see in the residual plot of figure 3.9. This means, that the resistance decreases with an increasing voltage and current.

Because it is not known, which range of the curve yields the correct quenching resistance, I introduce a systematic error on the resistance. This error is determined by first doing a fit in a range with a smaller slope. For the example in figure 3.9 the first fit is done between $73\,\text{V}$ and $74\,\text{V}$. Then a second fit is done in the range which has a larger slope, which corresponds to $74.5\,\text{V}$ to $75.5\,\text{V}$ in the example. The systematic error on the resistance is half of the difference between the parameters of the two fits.

As an average resistance I take the result of the fit over the whole range and the statistical errors on the average resistance are the errors of the fit parameters.

The analysis described above was done for all twelve SiPMs and the results are listed in table 3.4.

SiPM Type	n_{Pixels}	R_{meas} (Ω)	σ_R^{stat} (Ω)	σ_R^{sys} (Ω)
$1 \times 1\,\text{mm}^2$, $100\,\mu\text{m}$, 1549	100	2450	2	69
$1 \times 1\,\text{mm}^2$, $100\,\mu\text{m}$, 1550	100	2570	2	82
$1 \times 1\,\text{mm}^2$, $50\,\mu\text{m}$, 1926	400	1775	3	160
$1 \times 1\,\text{mm}^2$, $50\,\mu\text{m}$, 1927	400	1755	2	168
$1 \times 1\,\text{mm}^2$, $25\,\mu\text{m}$, 1067	1600	1195	4	65
$1 \times 1\,\text{mm}^2$, $25\,\mu\text{m}$, 1068	1600	1148	3	65
$3 \times 3\,\text{mm}^2$, $100\,\mu\text{m}$, 0551	900	665	3	0
$3 \times 3\,\text{mm}^2$, $100\,\mu\text{m}$, 0552	900	733	3	0
$3 \times 3\,\text{mm}^2$, $50\,\mu\text{m}$, 2888	3600	653	1	0
$3 \times 3\,\text{mm}^2$, $50\,\mu\text{m}$, 2889	3600	698	1	0
$3 \times 3\,\text{mm}^2$, $25\,\mu\text{m}$, 0149	14 400	438	1	10
$3 \times 3\,\text{mm}^2$, $25\,\mu\text{m}$, 0150	14 400	384	1	4

Table 3.4: This table lists the measured resistances, which were determined by linear regression on the characteristic I-V curves. The given systematic errors result from the uncertainties of the fitting range.
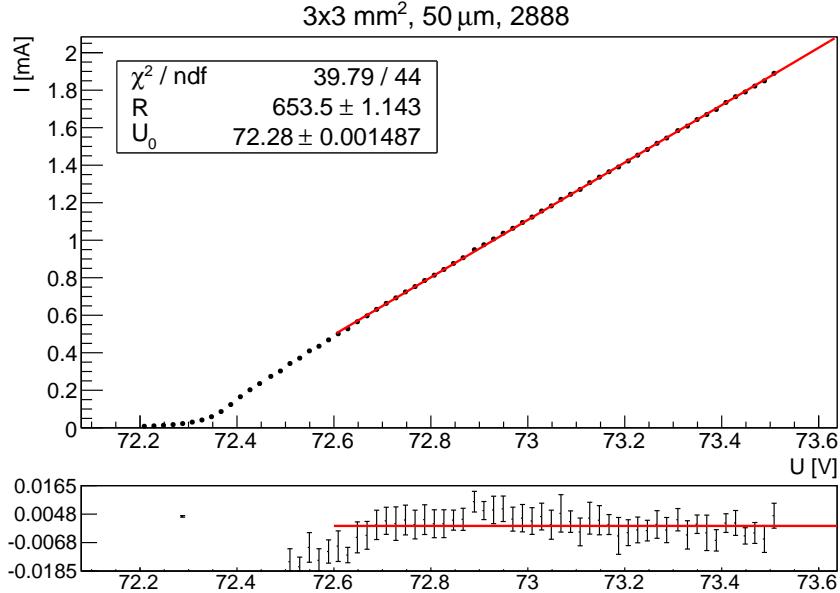
Figure 3.8: Linear fit on the characteristic curve with a high reverse bias voltage of the $3 \times 3\,\mathrm{mm}^2$, $50\,\mathrm{\mu m}$, 2888 SiPM. The current is linear and the fit results in an unambiguous value of $(653.5 \pm 1.1)\,\Omega$.
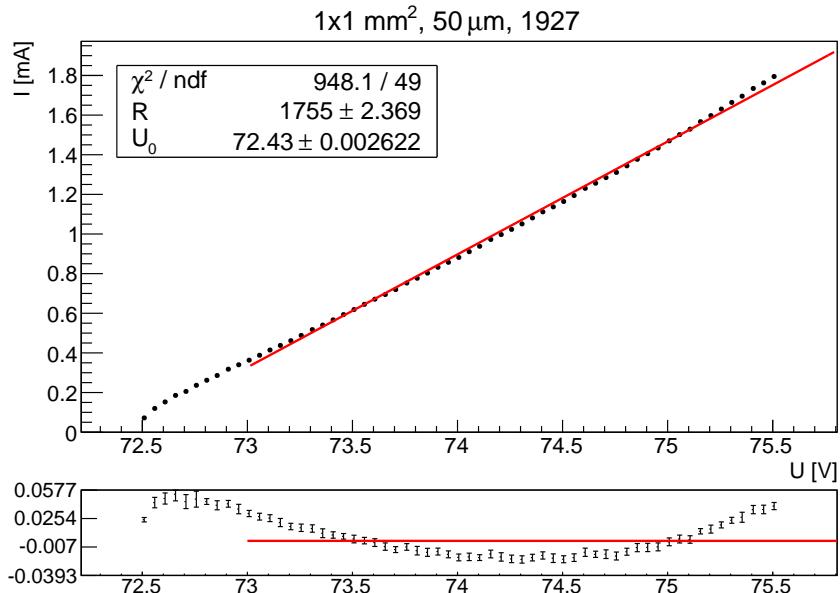

Figure 3.9: Linear fit on the characteristic curve with a high reverse bias voltage of the $1 \times 1\,\mathrm{mm}^2$, $50\,\mathrm{\mu m}$, 1927 SiPM. The current has a slight parabolic form which implies a falling resistance.

3.2.1. Determination of Bulk and Quenching Resistances

The next step is to determine the quenching resistance R_q from this results. For this we have to look at the electrical model of the SiPM as shown in figure 1.2. The whole resistance R_{meas} of the SiPM consists of the bulk resistance R_b and n parallel quenching resistors R_q, where n is the number of the SiPM's pixels. Thus, I get the following formula for R_{meas}:

$$R_{meas} = R_b + \frac{R_q}{n} \tag{3.2}$$

This explains why the measured resistance decreases with more pixels. The problem is, that I have one measured resistance for two resistance parameters for each SiPM, so I have to make two assumptions to determine the bulk and quenching resistances.

1. Every SiPM with the same bulk size of either $1 \times 1\,\text{mm}^2$ or $3 \times 3\,\text{mm}^2$ has the same bulk resistance $R_b^{1 \times 1}$ or $R_b^{3 \times 3}$.

2. The quenching resistance depends only on the pixel size and geometry, so SiPMs with the same pitch have the same quenching resistance R_q^{pitch}.

With these two assumptions I have five different resistances for my six types of SiPMs. For every SiPM type there is a different version of equation 3.2, so I have a system of six linear equations with 5 variables. I did measurements of two different SiPMs for each SiPM type, so I can use the average of the two measured resistances as values for R_{meas}.

These six equations can't be solved analytically, because the measured resistances are not exact, so there isn't any solution, which solves all six equations. However, I can try to determine the best solution of the equations, i.e. those resistances for which the right side of equation 3.2 is as close as possible to R_{meas}.

The first step is simplifying the equations by eliminating R_q. This yields three equations with the two variables $R_b^{1 \times 1}$ and $R_b^{3 \times 3}$. Finding the best solution for these three equations is equivalent to determining the values for which the following function becomes minimal:

$$\chi^2(R_b^{1 \times 1}, R_b^{3 \times 3}) = \sum_{i=1}^{3} \left(R_{meas}^i - 9R_{meas}^{i+3} - R_b^{1 \times 1} + 9R_b^{3 \times 3} \right)^2 \tag{3.3}$$

This is similar to a least-squares fit of a model to measured data points. Fortunately minimization of functions is a well-established numerical problem, for which several algorithms exist. I used SciPy's [28] implementation of the nonlinear conjugate gradient algorithm [29, p. 120-122] for minimizing 3.3.

The resulting parameters for the found minimum are $R_b^{1 \times 1} \approx 460\,\Omega$ and $R_b^{3 \times 3} \approx 450\,\Omega$, which results in the quenching resistances listed in table 3.5.

The determined resistances can be only rough estimates, because it is unclear how accurate the used assumptions are. In addition, three data points are normally not sufficient for a good least-squares minimization with two parameters, because the minimization has only one degree of freedom.

3.2.2. Forward Bias

Another problem is, that the resistance of the diode probably isn't negligible as a constant avalanche is needed to make the diode conducting in reverse bias. So as a consistency check a few measurements with a forward bias voltage were performed.

These measurements showed also the aforementioned quadratic relation between current and voltage, so the resistance decreases linearly with the current, as you can see in figure 3.10. One reason for this non-Ohmic behaviour could be a locally rising temperature of the SiPM due to the current. The temperature dependance of the semiconductor resistance is exponential [5, p. 488] though, so this doesn't explain the linear behaviour of the resistance. There are papers which report a voltage-dependant characteristic for polysilicon resistors, which are also used in SiPMs [30, 31].

The measured resistance of the forward biased SiPM doesn't match the resistance in table 3.4 most of the time. For example figure 3.10 shows a resistance between $250\,\Omega$ and $450\,\Omega$ while the same $1 \times 1\,\mathrm{mm}^2$, $25\,\mu\mathrm{m}$ SiPM has a resistance of $(1195 \pm 65)\,\Omega$ in reverse bias, so the measured resistance in forward bias is significantly lower.
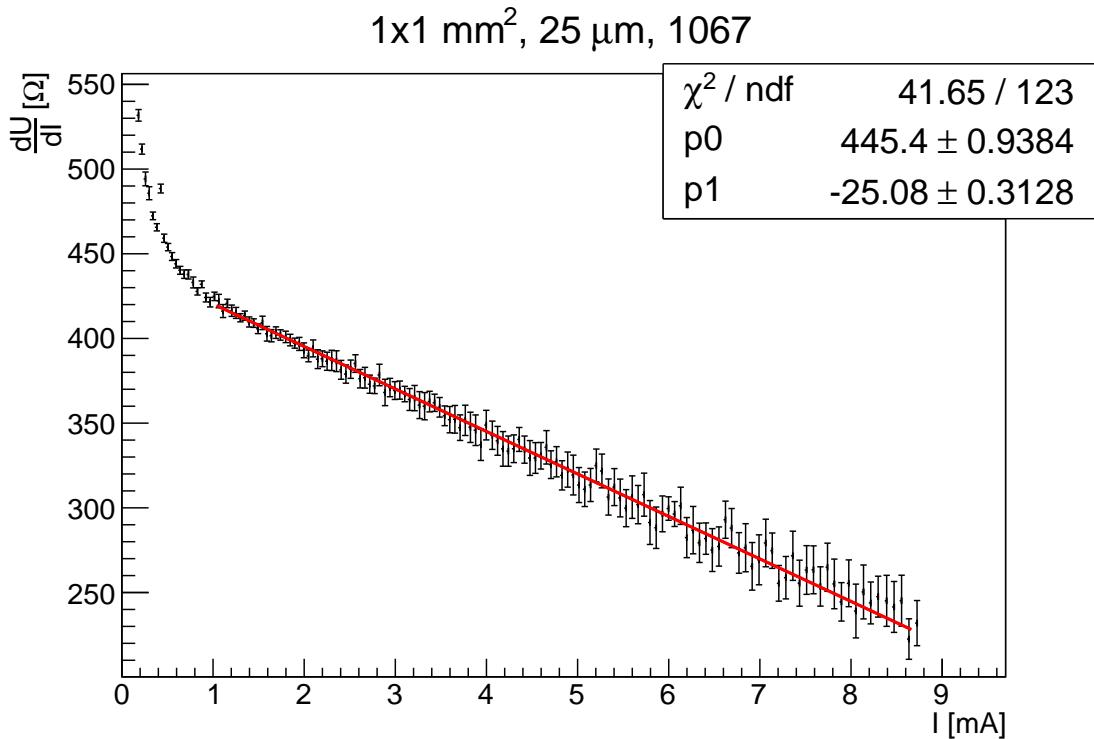

Figure 3.10: Resistance of the $1 \times 1\,\mathrm{mm}^2$, $25\,\mu\mathrm{m}$, 1067 SiPM. The measurements were done with a forward biased SiPM and the resistance was determined by numerically calculating $\frac{dU}{dI}$. Surprisingly the resistance is not constant but depends on the current and the applied voltage.

Measurements with other SiPMs showed a higher resistance in forward bias, as for example the $1 \times 1 \, \text{mm}^2$, $100 \, \mu\text{m}$ SiPM, whose measured resistance was approximately $3000 \, \Omega$ in forward bias and $(2450 \pm 69) \, \Omega$ in reverse bias at the same current.

All of this shows, that the above determined values for R_q and R_b are only rough estimates. Further research is needed to understand the inconsistencies between forward and reverse biased and the voltage dependance of the polysilicon resistors. However, this would go beyond the scope of this thesis, so a first estimate of these values must suffice.

3.3. Determination of SiPM Capacitances

The pixel capacitances can be determined from the previous determined quenching resistances and the pixel recovery times with $C = \tau_1 / R_q$ as formula 1.1 implies. For the pixel recovery time τ_1 I take the values from the peak-to-tail fits and calculate the mean of the range in table 3.1. The quenching resistance is determined as described in the previous section and the used quenching resistance for the different pixel sizes is given in table 3.5.

It is expected, that the capacitance per active pixel area C/A_p is approximately constant, because the same silicon material is used for each SiPM type and each SiPM type has the same lateral pixel size. Therefore, the capacitance per pixel area can be used to do a useful consistency check, because I know that the determined resistances are inaccurate. The active pixel area A_p is the product of the pitch size and the geometrical fill factor, which is given by the manufacturer.

Another consistency check is the terminal capacitance, which is given by the manufacturer as $35 \, \text{pF}$ for the $1 \times 1 \, \text{mm}^2$ SiPMs and $320 \, \text{pf}$ for the $3 \times 3 \, \text{mm}^2$. The terminal capacitance is the overall capacitance of all pixels, so it is the product of the pixel capacitance and the number of pixels. I suppose though, that the manufacturer didn't actually measure the terminal capacitance but rather calculated it using the known material and geometrical properties of the SiPM. Hence, the given terminal capacitance may be inaccurate and shouldn't be trusted too much.

SiPM Type	R_q (kΩ)	C_{Pixel} (fF)	C/A_p (pF/mm^2)	$C_{Terminal}$ (pF)
$1 \times 1 \, \text{mm}^2$, $100 \, \mu\text{m}$	205	200	26	20
$1 \times 1 \, \text{mm}^2$, $50 \, \mu\text{m}$	521	27	17	11
$1 \times 1 \, \text{mm}^2$, $25 \, \mu\text{m}$	1136	7	38	12
$3 \times 3 \, \text{mm}^2$, $100 \, \mu\text{m}$	205	232	30	209
$3 \times 3 \, \text{mm}^2$, $50 \, \mu\text{m}$	521	37	24	134
$3 \times 3 \, \text{mm}^2$, $25 \, \mu\text{m}$	1136	10	53	146

Table 3.5: Capacitances of different SiPM types. The determined pixel capacitances can only be regarded as rough estimates, because the quenching resistances have a very high systematic uncertainty. The capacitance per pixel area should be approximately constant, so this indicates that the determined capacitance for the SiPMs with $25 \, \mu\text{m}$ pitch is probably too high.

Table 3.5 lists the determined pixel capacitances. The capacitance drops more than expected between the SiPMs with 100 µm and 50 µm pitches and less than expected between the SiPMs with 50 µm and 25 µm pitches, as the capacitance per area shows. The reason for this is probably an inaccurate value for the quenching resistance. The determination of the quenching resistance becomes more difficult for higher number of pixels, because the relative influence of the bulk resistance increases.

The determined terminal capacitance is smaller than the manufacturer's value, but of the same order of magnitude. This can be interpreted as a validation that the determined capacitances have the correct order of magnitude, but the exact values should not be trusted. The correct quantitative determination of the pixel capacitances would require a better understanding of the pixel resistances, which was not feasible during the short time of this thesis.

3.4. Overvoltage Dependance of the Recovery Time

The recovery time of the $3 \times 3 \, \mathrm{mm}^2$, 50 µm SiPM was measured at different bias voltages to investigate the overvoltage dependance of the recovery time. The peak-to-tail data was analysed as described in 3.1.2 and the breakdown voltage was determined from the characteristic I-V curve of the SiPM (see section 3.2).

Figure 3.11 shows the recovery time τ_1 as a function of the applied overvoltage. There is a significant increase in τ_1 when increasing the overvoltage. Linear fits show, that the recovery time increases by something between 1 ns/V and 2 ns/V in the measured range.

The breakdown voltage of the SiPM depends linearly on the temperature with a slope of $\beta \approx 0.06 \, \mathrm{V/K}$ [25, 32]. This effect causes a temperature dependance of τ_1 of approximately $-0.1 \, \mathrm{ns/K}$. This could explain the discrepancies of about 0.5 ns for this SiPM between different measurements of the recovery time as discussed in section 3.1.2, as such a change of the recovery time could be caused by a change in the temperature of 5 K, which is not unrealistic. However, this is not the only source of temperature dependance, but it may be the most significant.

Another known source of temperature dependance is the temperature dependance of the polysilicon quenching resistors. The resistance of semiconductors decreases with the temperature, so this should also decrease the recovery time, which is $\tau = R{\cdot}C$. Therefore, this effect adds to the overvoltage dependance, which implies that the overall recovery time decreases with rising temperature.

The linear temperature dependance of the breakdown voltage could be compensated by adjusting the bias voltage, so that the overvoltage stays constant. With such a control system one could investigate the temperature dependance of the recovery time without a bias by the overvoltage dependance and quantify how much the overvoltage dependance of the recovery time contributes to the overall temperature dependance.

The bulk recovery time τ_2 increases faster with the overvoltage, as figure 3.12 indicates. Linear fits with different ranges show an increase of τ_2 by something between 75 ns/V and 90 ns/V.

One possible reason for the overvoltage dependance of the recovery time is an increased

number of afterpulses, which interrupt the recovery of an SiPM cell and thus increase the overall SiPM recovery time (see section 1.2.3.3). The size of the avalanches increases with the overvoltage, so with increasing overvoltage more deep level traps in the pixel are filled, which causes more afterpulses when the trapped charge carriers are released [22].

This model also explains the beginning of a saturation in figure 3.11 and 3.12. The avalanche can't grow larger than the full pixel size, so at some overvoltage the maximal avalanche size is reached and thus the number of filled charge carrier traps can't increase anymore.
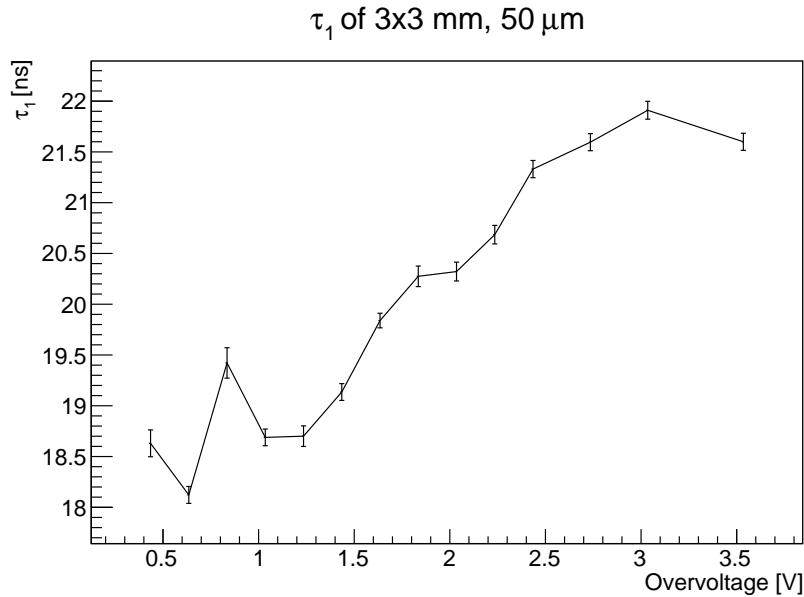

Figure 3.11: Overvoltage dependance of the pixel recovery time constant τ_1. The overvoltage has a systematic error of ± 0.1 V.
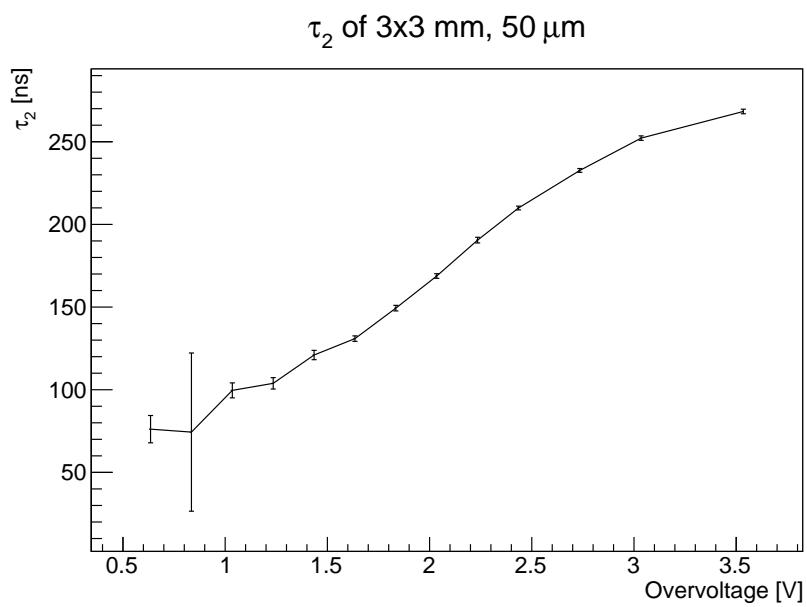
Figure 3.12: Overvoltage dependance of the bulk recovery time constant τ_2. The overvoltage has a systematic error of ± 0.1 V.

4. Summary and Outlook

The recovery times of seven different SiPM types have been determined. Two LEDs were used to first fire the whole SiPM with a blinding light pulse and then after a variable time delay flash it with a probing light pulse. Both SiPM pulses were measured with an oscilloscope.

The LEDs have proven to have a sufficient brightness and bandwidth to fire nearly all pixels of the SiPM with a pulse width of approximately 5 ns. The limiting factor with regards to bandwidth and amplitude was the arbitrary function generator, so shorter and higher pulses might be possible with a different pulse source.

An issue was the unwanted electrical coupling between the LEDs and the SiPMs, which distorted the SiPM pulses. Separating the LEDs and the SiPM using fibers for the light transport reduced this distortions to a minimum, but unfortunately the light flux via fiber wasn't longer sufficient for blinding the larger SiPMs. Maybe with higher pulse amplitudes one could perform all measurement with the fiber, which would greatly reduce systematic deviations from the ideal pulse models.

The first observation was, that the absolute pulse amplitude of the second SiPM pulse stays nearly constant, when the time difference between the two light pulses is reduced until the two pulses become undistinguishable. However, SiPM pulses have a tail, so the peak-to-tail amplitude of the second pulse decreases significantly when the time difference is reduced.

To analyze this decrease, the ratio of the peak-to-peak amplitude of the two pulses was plotted as a function of the time difference and the superposition of two exponential function was fitted to the peak-to-peak ratio, because there are two time constants in the recovery process of the SiPM. The fast and dominating recovery time can be assigned to the recharge of the SiPM pixels and the slow recovery time can be assigned to the recharge of the SiPM bulk. The pixel recovery time attributes to more than 90% of the recovery process, while the bulk recovery time dominates the tail of the recovery process. The bulk recovery time is more dominant for SiPMs with large pitches.

The same fits have been made on the tails of the SiPM pulses which resulted in slightly lower recovery times. However, the systematic uncertainties for these fits are large due to difficulties in the choice of the fit ranges. The oscillations on top of the pulses due to coupling between the LED and the SiPM cause a too large χ^2 and complicate the fit process.

Plots of the ratio of the absolute pulse heights showed a small decrease by about 5 % for the SiPMs with 100 μm and 50 μm pitches. Fits of exponential function resulted in approximately the same recovery time as the peak-to-tail analysis. The SiPM by KETEK was the only SiPM for which a significant decrease in absolute pulse height by about 50 % was observed. Both recovery times of this SiPM are over four times higher than the

recovery times of the SiPMs by HAMAMATSU with the same geometry. Additionally, the bulk recovery time is more dominating for this SiPM.

In order to determine the pixel capacitances from the pixel recovery times the quenching resistances had to be determined, because the pixel capacitance is recharged via quenching resistors. The effective resistance of the SiPM was determined by measuring the SiPM's characteristic I-V curves above the breakdown voltage. The determined resistances have high and partially unknown systematic uncertainties, because a voltage dependance of the resistance has been observed. Additionally the measurements of the resistance in forward and in reverse bias were partially inconsistent. A few assumptions had to be made to determine the bulk resistance and the quenching resistances from the measured effective resistance. This yielded a system of linear equations which were solved by least-square minimization. This method introduced additional uncertainties.

In conclusion, the determination of the quenching resistances is inaccurate and must only be regarded as a rough estimation. Further research is needed to determine the internal resistances of the SiPMs.

The pixel capacitance has been determined to approximately $10\,\mathrm{fF}$ to $200\,\mathrm{fF}$, depending on the pixel size. The capacitance per active pixel area is in the order of approximately $30\,\mathrm{pF/mm^2}$. These values are only rough estimates as well, since the determination of the capacitances depends on the resistances.

The pixel recovery time decreases when only part of the SiPM's pixels fire. The recovery times increase when the overvoltage is increased. This introduces a temperature dependance of the recovery time, because the breakdown voltage increases linearly with the temperature. Another source of temperature dependance of the recovery time is the temperature dependance of the polysilicon quenching resistors. This implies a decrease in the recovery time with rising temperature.

The temperature dependance of the recovery time was a large problem. Repeating measurements on the next day often produced results which had a discrepancy of several σ to previous measurements. Therefore, only ranges of measured recovery times were given for each SiPM type. The statistical precision of the recovery time was mostly below $1\,\%$. Therefore, the determination of the recovery time with a precision of $0.1\,\mathrm{ns}$ could be possible in a temperature controlled environment. Further research is required to quantify the temperature dependance of the recovery time.

Another interesting point of research is the first part of the pulse. Before the tail starts, there are structures in the pulse shape, which could perhaps be explained by the parasitic quenching capacitance and by the pulse width of the LED. This has to be studied to achieve a better understanding of the electrical model and parameters of the SiPM. The goal should be, to experimentally verify the presented electrical model in figure 1.2 and to develop measurements for determining all parameters of this model.

A. Tables

SiPM Type	Gate	τ_1 (ns)	$\sigma_{\tau_1}^{stat}$ (ns)	$\sigma_{\tau_1}^{fit}$ (ns)	τ_2 (ns)	$\sigma_{\tau_2}^{stat}$ (ns)	$\sigma_{\tau_2}^{fit}$ (ns)	t_1 (ns)	$\sigma_{t_1}^{stat}$ (ns)	$\sigma_{t_1}^{fit}$ (ns)	t_2 (ns)	$\sigma_{t_2}^{stat}$ (ns)	$\sigma_{t_2}^{fit}$ (ns)
11-100-1549	narrow	43.0	0.5	0.4	188	13	2	27.5	0.3	0.2	−390	43	3
11-100-1549	narrow	40.0	1.1	0.7	132	8	6	24.5	0.3	0.3	−190	26	18
11-100-1549	moderate	39.4	0.7	0.7	154	7	8	24.2	0.2	0.3	−258	23	25
11-100-1549	wide	37.5	2.0	0.4	165	25	5	28.3	0.7	0.2	−338	47	14
11-100-1549	wide	41.2	1.7	0.6	115	13	6	27.4	0.4	0.3	−141	46	19
11-100-1550	narrow	44.7	2.0	0.5	203	36	7	28.3	0.7	0.2	−338	47	14
11- 50-1926	narrow	13.6	0.1	0.1	79	23	5	32.3	0.1	0.1	−246	84	22
11- 50-1926	moderate	13.5	0.1	0.1	96	5	4	32.6	0.1	0.1	−294	24	20
11- 50-1926	wide	14.1	0.1	0.1	111	3	5	32.0	0.1	0.1	−363	15	21
11- 50-1927	narrow	13.5	0.2	0.1	93	7	5	32.5	0.2	0.1	−273	32	20
11- 50-1927	moderate	13.7	0.1	0.1	104	4	5	32.4	0.1	0.1	−326	16	22
11- 50-1927	wide	14.0	0.1	0.1	89	7	4	32.0	0.1	0.1	−265	29	19
11- 25-1068	narrow	7.9	0.1	0.1	47	23	4	24.8	0.1	0.1	−155	115	21
11- 25-1068	moderate	8.1	0.0	0.1	116	9	12	24.9	0.0	0.1	−538	50	63
11- 25-1068	moderate	7.9	0.1	0.1	79	6	7	24.8	0.1	0.1	−321	32	39
11- 25-1068	wide	8.1	0.0	0.1	107	4	10	24.9	0.0	0.1	−473	21	54
11- 25-1068	wide	8.8	0.0	0.1	144	19	12	23.8	0.1	0.1	−719	106	65
11- 25-1067	narrow	7.6	0.1	0.1	41	23	2	25.1	0.1	0.1	−131	115	13
11- 25-1067	moderate	8.1	0.0	0.1	102	17	9	24.6	0.1	0.1	−467	89	50
11- 25-1067	wide	8.3	0.1	0.1	52	10	5	24.3	0.1	0.1	−203	49	27
33-100-0551	moderate	46.4	0.1	0.2	217	3	3	26.6	0.1	0.1	−419	10	9
33-100-0551	wide	47.8	0.2	0.2	229	4	3	25.9	0.1	0.1	−454	13	9
33-100-0552	narrow	46.2	0.1	0.2	218	2	3	26.9	0.1	0.1	−439	8	10
33-100-0552	moderate	47.2	0.1	0.1	219	1	2	26.9	0.0	0.0	−450	5	5
33-100-0552	wide	48.9	0.1	0.2	236	4	4	25.8	0.1	0.1	−513	13	12
33- 50-2888	narrow	19.1	0.2	0.1	96	5	2	33.2	0.1	0.1	−257	21	8
33- 50-2888	moderate	19.8	0.1	0.1	125	2	2	32.8	0.1	0.1	−375	11	11
33- 50-2888	wide	19.8	0.1	0.1	121	2	2	33.1	0.1	0.1	−363	8	10
33- 50-2889	narrow	19.1	0.1	0.1	106	3	2	33.1	0.1	0.1	−309	14	9
33- 50-2889	moderate	19.3	0.2	0.1	129	7	3	32.9	0.2	0.1	−412	30	13
33- 50-2889	wide	19.1	0.0	0.0	105	1	1	32.3	0.0	0.1	−305	5	5
33- 25-0149	narrow	11.5	0.1	0.1	142	17	7	29.4	0.1	0.1	−696	94	38
33- 25-0149	moderate	11.5	0.0	0.1	143	7	8	29.6	0.1	0.1	−702	38	45
33- 25-0149	moderate	11.1	0.0	0.1	86	2	3	30.1	0.1	0.1	−371	13	20
33- 25-0149	wide	11.8	0.1	0.1	106	4	8	29.3	0.1	0.1	−484	26	44
33- 25-0150	narrow	11.7	0.1	0.1	154	57	7	29.1	0.1	0.1	−809	322	40
33- 25-0150	moderate	11.5	0.1	0.1	144	44	7	29.7	0.1	0.1	−767	238	42
33- 25-0150	wide	12.0	0.0	0.1	127	16	9	29.1	0.1	0.1	−605	95	52
33-Ketek	narrow	83.0	0.4	0.4	451	23	21	7.9	0.2	0.2	−897	53	49
33-Ketek	moderate	83.3	0.1	0.3	482	8	16	7.2	0.1	0.1	−960	18	36
33-Ketek	wide	83.7	0.2	0.3	481	12	15	7.0	0.1	0.1	−967	28	35

Table A.1: Fit parameters of the peak-to-tail data.

SiPM Type	Fit Range	τ_1 (ns)	$\sigma_{\tau_1}^{stat}$ (ns)	τ_2 (ns)	$\sigma_{\tau_2}^{stat}$ (ns)	t_1 (ns)	$\sigma_{t_1}^{stat}$ (ns)	t_2 (ns)	$\sigma_{t_2}^{stat}$ (ns)
11-100	moderate	37.3	0.8	117	6	−67.6	2.7	−579	43
11-100	moderate	37.0	0.4	106	8	−67.2	1.3	−501	55
11-100	moderate	37.5	0.6	122	5	−68.6	2.1	−611	37
11-100	moderate	37.8	0.6	121	7	−69.3	2.3	−595	48
11-100	wide	41.8	0.3	155	15	−85.2	0.7	−867	101
11-100	wide	40.6	0.3	150	20	−80.5	1.0	−811	131
11-100	wide	40.4	0.3	138	12	−80.8	1.1	−729	79
11-100	wide	40.9	0.3	163	9	−81.3	1.2	−898	58
11-100	narrow	35.9	0.9	97	6	−63.3	3.3	−425	42
11-100	narrow	34.5	0.6	94	7	−58.2	2.0	−406	50
11-100	narrow	35.2	0.9	101	7	−60.2	3.2	−458	51
11-100	narrow	36.6	0.9	116	10	−64.8	3.4	−559	69
11-50	moderate	12.3	0.4	71	6	25.8	1.2	−333	37
11-50	moderate	12.4	0.3	51	19	25.6	0.9	−218	109
11-50	wide	13.1	0.1	142	13	22.5	0.3	−734	75
11-50	wide	13.2	0.3	138	17	22.4	0.7	−717	97
11-50	narrow	11.1	0.7	62	16	32.6	3.5	−285	89
11-50	narrow	11.0	1.7	42	12	32.0	8.8	−159	77
11-25	moderate	6.7	0.1	32	2	40.4	0.3	−114	10
11-25	moderate	6.9	0.1	41	2	39.4	0.3	−169	15
11-25	wide	7.1	0.0	56	4	39.1	0.1	−262	23
11-25	wide	7.2	0.0	65	4	38.8	0.1	−309	25
11-25	narrow	6.0	0.3	32	2	44.5	1.5	−107	12
11-25	narrow	5.9	0.4	28	6	44.1	2.2	−84	39
33-100	moderate	47.8	0.1			−35.4	0.2		
33-100	wide	50.3	0.1			−40.4	0.1		
33-100	narrow	43.1	0.3			−26.6	0.6		
33-50	moderate	18.5	0.1	86	16	42.6	0.1	−258	61
33-50	wide	18.9	0.1	128	22	41.9	0.1	−449	80
33-50	narrow	17.6	0.3	61	4	43.9	0.4	−147	20
33-25	moderate	11.0	0.1	58	10	54.0	0.1	−181	45
33-25	wide	11.3	0.0	132	13	53.5	0.0	−491	52
33-25	narrow	10.4	0.3	32	13	55.1	0.5	−156	60
KETEK	moderate	83.8	0.3	762	12	20.3	0.5	−1338	20
KETEK	wide	76.9	0.3	625	7	31.6	0.4	−1077	14
KETEK	narrow	96.0	0.7	1159	39	−2.2	1.1	−1976	56

Table A.2: Fit parameters of the pulse tails. The fit range is not well-defined, so fits for three reasonable ranges were done, as written in the second column. The resulting systematic errors due to the fitting range outweigh the statistical errors.

SiPM Type	Gate	τ_1 (ns)	$\sigma_{\tau_1}^{stat}$ (ns)	$\sigma_{\tau_1}^{fit}$ (ns)	τ_2 (ns)	$\sigma_{\tau_2}^{stat}$ (ns)	$\sigma_{\tau_2}^{fit}$ (ns)	t_1 (ns)	$\sigma_{t_1}^{stat}$ (ns)	$\sigma_{t_1}^{fit}$ (ns)	t_2 (ns)	$\sigma_{t_2}^{stat}$ (ns)	$\sigma_{t_2}^{fit}$ (ns)
11-100-1549	narrow	46.2	2.5	1.0	112	73	4	−38.2	4.0	2.4	−256	308	15
11-100-1549	narrow	37.8	4.6	1.4	101	24	4	−35.1	10.7	3.7	−217	112	14
11-100-1549	wide	55.4	3.0	1.0	112	279	5	−55.8	5.6	2.7	−274	936	20
11-100-1550	narrow	41.8	3.5	1.5				−90.8	13.5	5.9			
11- 50-1926	narrow	12.0	0.4	0.2				12.5	1.3	0.8			
11- 50-1926	moderate	12.6	0.3	0.2				10.7	0.8	0.8			
11- 50-1926	wide	11.9	0.2	0.2				13.2	0.6	0.7			
11- 50-1927	narrow	12.1	0.2	0.2				12.7	0.8	0.8			
11- 50-1927	moderate	12.6	0.2	0.2				11.1	0.6	0.8			
11- 50-1927	wide	13.1	0.3	0.3				9.5	0.9	0.8			
33-100-0551	moderate	37.0	0.7	0.5	157	7	3	−24.8	1.1	1.0	−482	31	15
33-100-0551	wide	41.9	1.1	0.8	153	11	7	−38.1	1.7	1.2	−452	50	33
33-100-0552	narrow	40.0	0.4	0.5	156	7	4	−31.2	0.6	1.0	−531	34	21
33-100-0552	moderate	44.6	0.4	0.2	205	6	2	−38.0	0.7	0.3	−782	30	12
33-100-0552	wide	52.9	0.5	0.2	379	72	7	−57.7	1.2	0.5	−1878	317	33
33- 50-2888	narrow	18.8	0.4	0.2				−5.8	1.5	0.6			
33- 50-2888	moderate	18.8	0.2	0.2				−6.3	0.6	0.6			
33- 50-2888	wide	17.8	0.1	0.2				−2.6	0.5	0.6			
33- 50-2889	moderate	15.6	0.2	0.2				1.7	0.8	0.7			
33- 50-2889	wide	16.1	0.1	0.1				−0.4	0.2	0.3			
33- 50-Ketek	narrow	95.2	0.1	0.1				−33.5	0.1	0.2			
33- 50-Ketek	moderate	95.5	0.1	0.1				−34.3	0.1	0.1			
33- 50-Ketek	wide	95.5	0.1	0.1				−34.4	0.1	0.1			

Table A.3: Fit parameters of the absolute pulse height data. For the rows with empty cells a single exponential function was fitted, so there is only one time parameter. There was only a slight decrease in the pulse height, so these fits are very sensitive to any perturbation. For SiPMs with 25 μm pitch no decrease could be observed.

B. Additional Plots
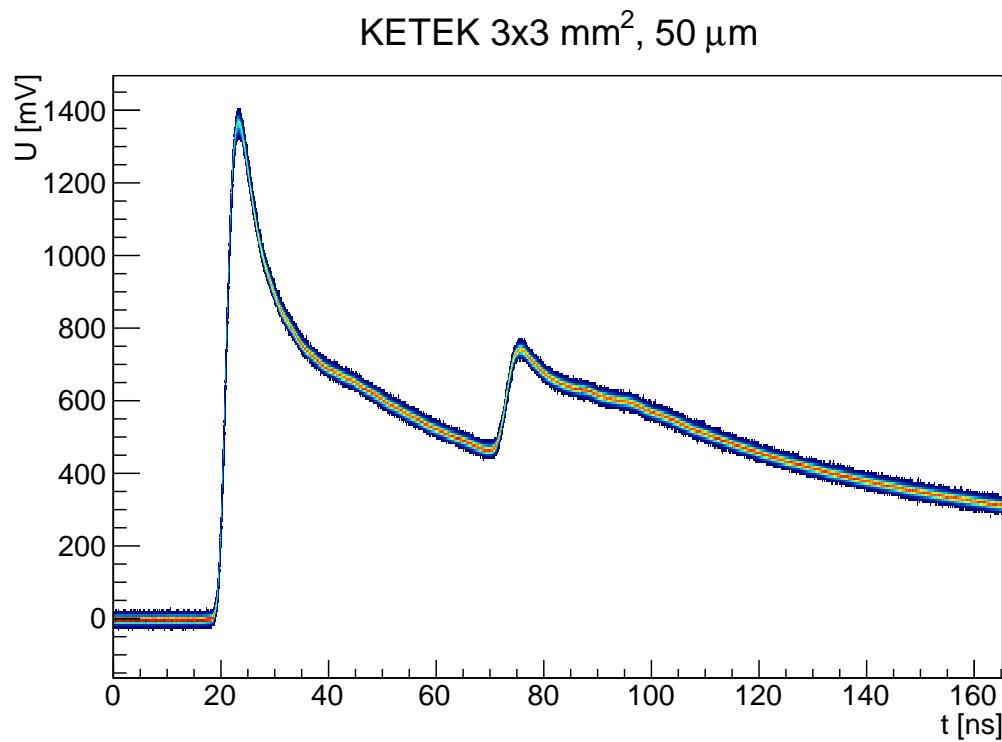
Figure B.1: Two KETEK SiPM pulses with a time difference of $\Delta t = 50\,\text{ns}$. The pulse height of the second pulse is significantly reduced in contrast to the pulses of the HAMAMATUS SiPM in figure 3.1.

B.1. Peak-to-Tail Pulse Ratio
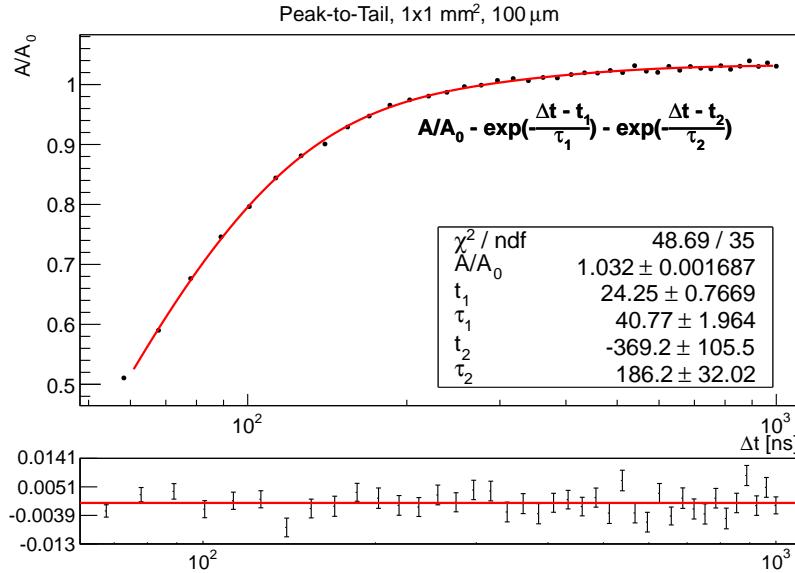
Figure B.2: Peak-to-tail ratio of the $1 \times 1\,\mathrm{mm}^2$, $100\,\mu\mathrm{m}$ SiPM pulses with the fit of two superpositioned exponential functions.
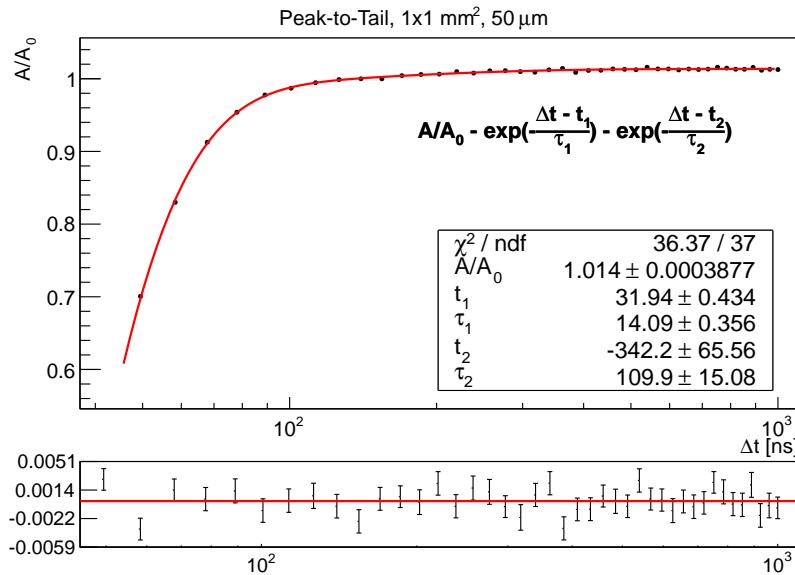

Figure B.3: Peak-to-tail ratio of the $1 \times 1\,\mathrm{mm}^2$, $50\,\mu\mathrm{m}$ SiPM pulses with the fit of two superpositioned exponential functions.
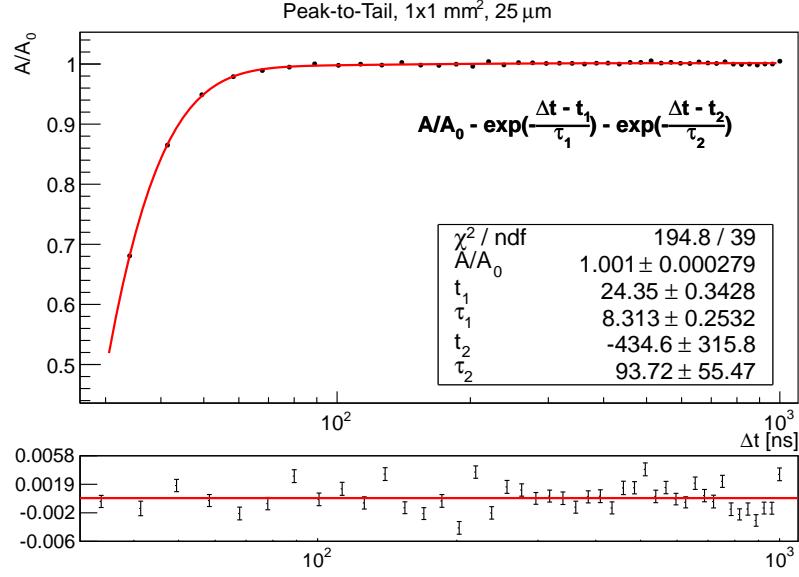
Figure B.4: Peak-to-tail ratio of the $1 \times 1\,\mathrm{mm}^2$, $25\,\mu\mathrm{m}$ SiPM pulses with the fit of two superpositioned exponential functions.
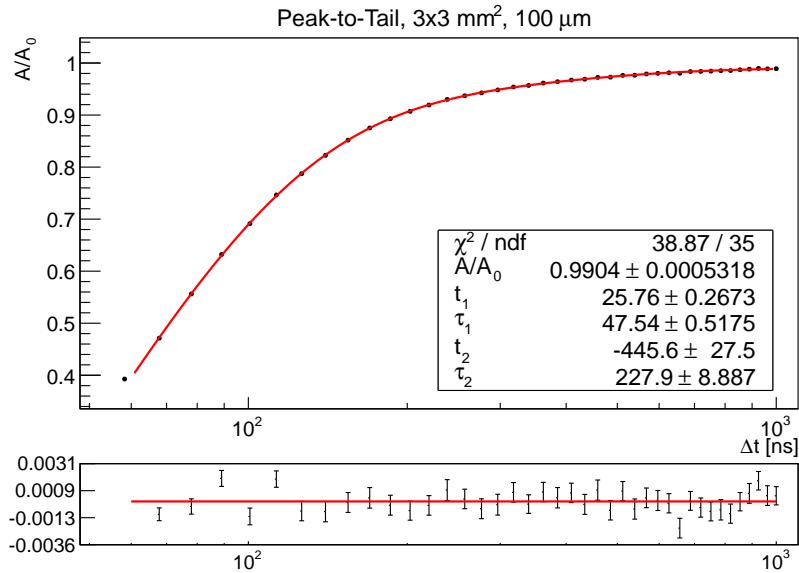
Figure B.5: Peak-to-tail ratio of the $3 \times 3\,\mathrm{mm}^2$, $100\,\mu\mathrm{m}$ SiPM pulses with the fit of two superpositioned exponential functions.
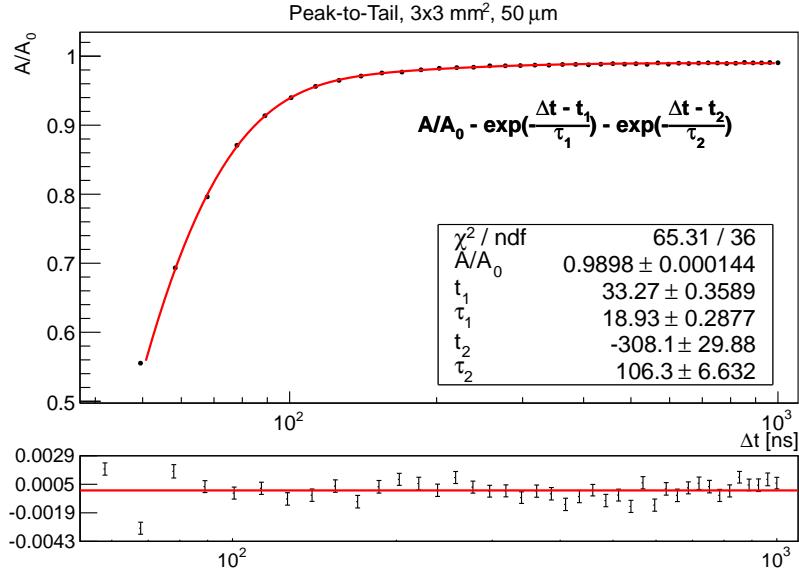
Figure B.6: Peak-to-tail ratio of the $3 \times 3\,\mathrm{mm}^2$, $50\,\mathrm{\mu m}$ SiPM pulses with the fit of two superpositioned exponential functions.
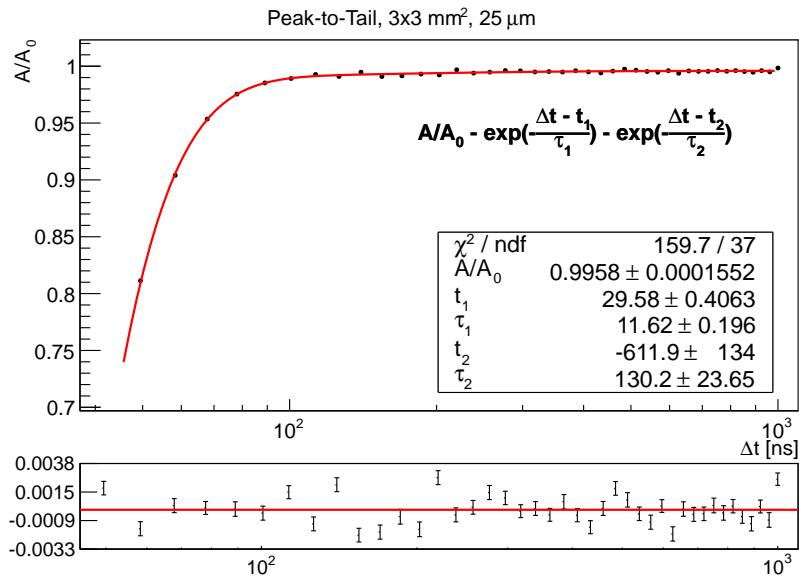
Figure B.7: Peak-to-tail ratio of the $3 \times 3\,\mathrm{mm}^2$, $25\,\mathrm{\mu m}$ SiPM pulses with the fit of two superpositioned exponential functions.
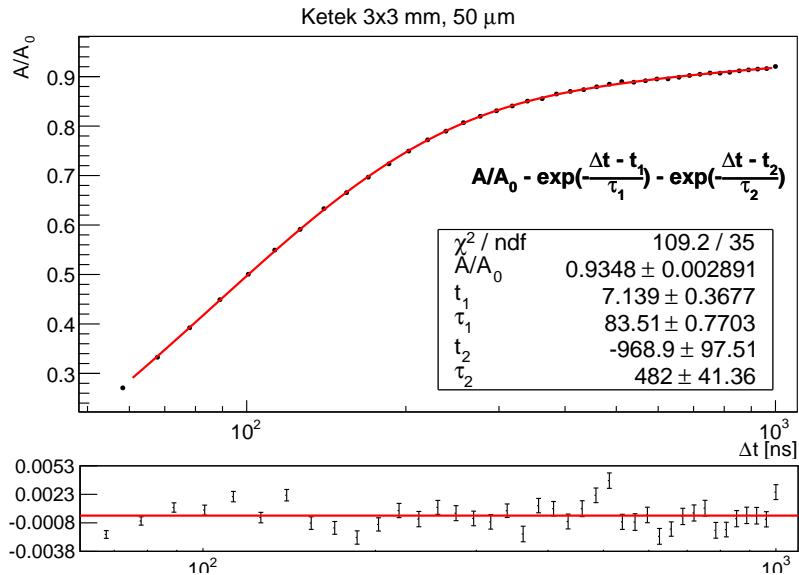
Figure B.8: Peak-to-tail ratio of the $3 \times 3\,\mathrm{mm}^2$, $50\,\mu\mathrm{m}$ KETEK SiPM pulses with the fit of two superpositioned exponential functions.

B.2. Pulse Tail
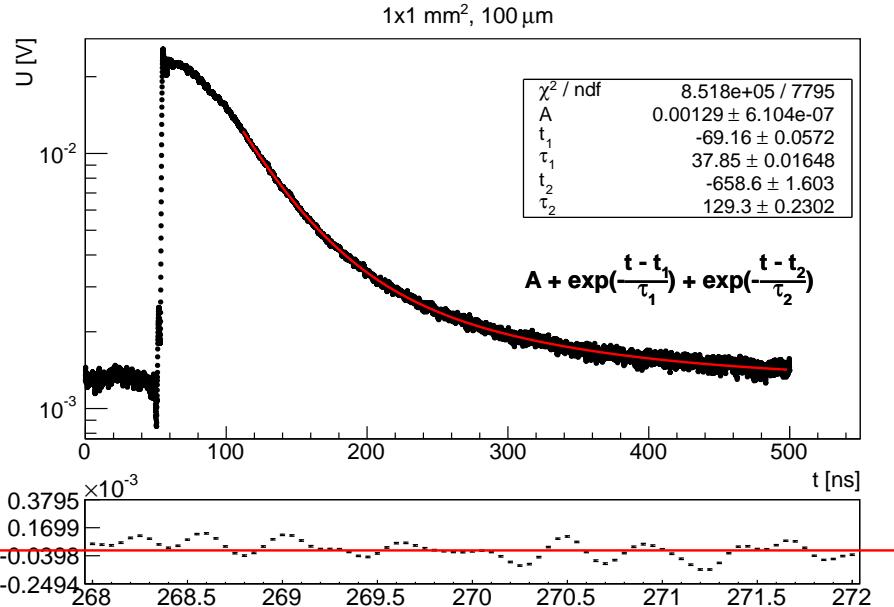
Figure B.9: Fit on the pulse tail of the $1 \times 1 \, \text{mm}^2$, $100 \, \mu\text{m}$ SiPM. The zoomed in residuals show the systematic oscillations on the pulse, which have been observed for every pulse. The data is the average of 200 measured pulses, which shows that the oscillations are stable and systematic. These systematics are the reason for the much too large χ^2/ndf and the underestimated errors on the fit parameters.
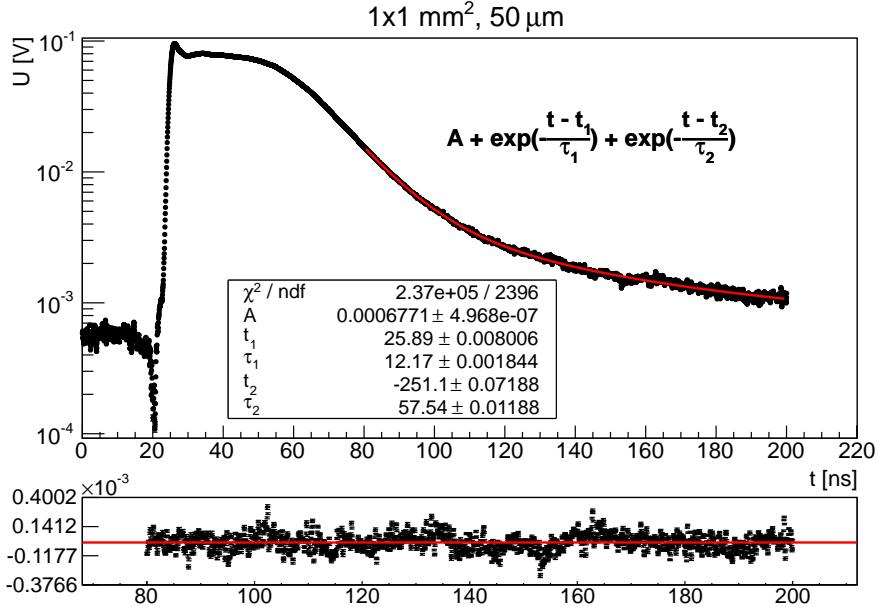
Figure B.10: Fit on the pulse tail of the $1 \times 1\,\mathrm{mm}^2$, $50\,\mu\mathrm{m}$ SiPM. The plotted SiPM pulse is the average of 200 pulses.
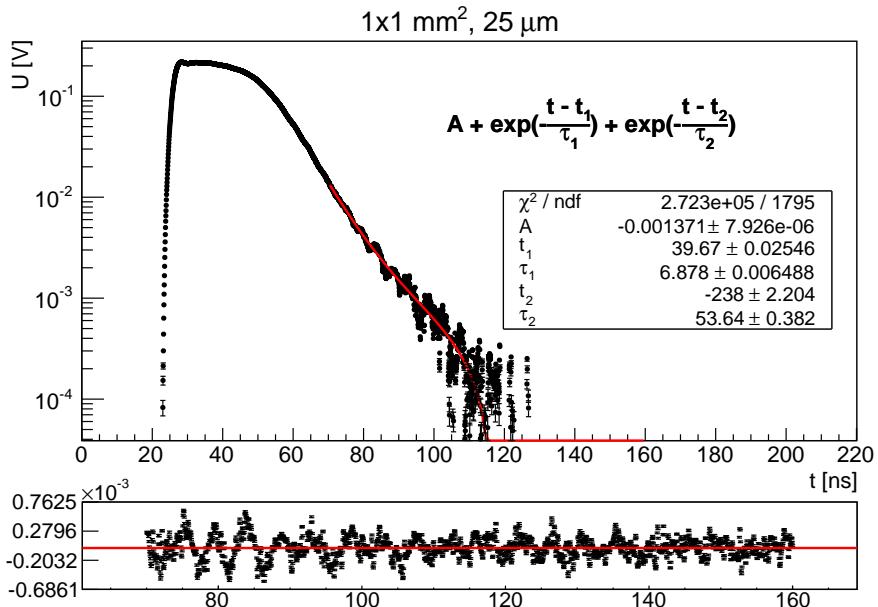
Figure B.11: Fit on the pulse tail of the $1 \times 1\,\mathrm{mm}^2$, $25\,\mu\mathrm{m}$ SiPM. The plotted SiPM pulse is the average of 200 pulses.
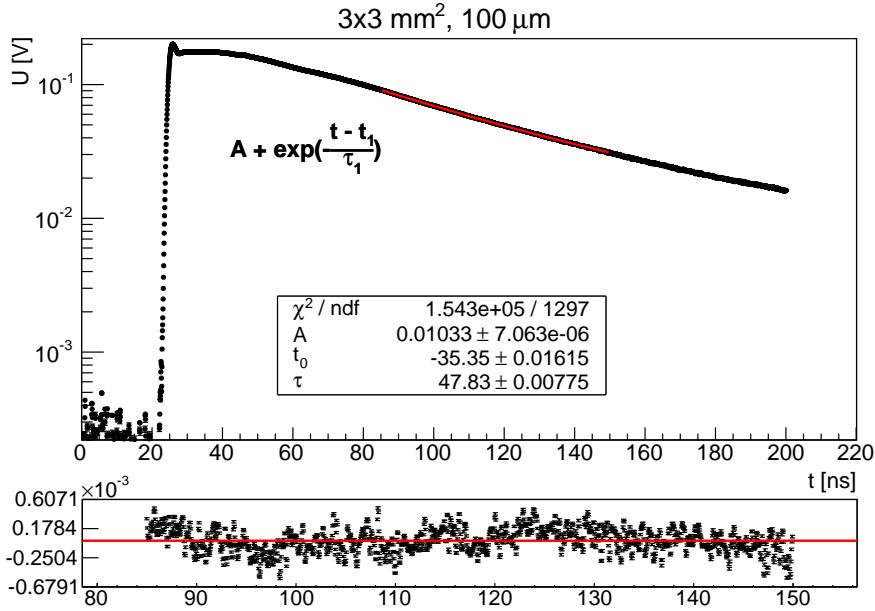
Figure B.12: Fit on the pulse tail of the $3 \times 3\,\mathrm{mm}^2$, $100\,\mu\mathrm{m}$ SiPM. The plotted SiPM pulse is the average of 200 pulses.
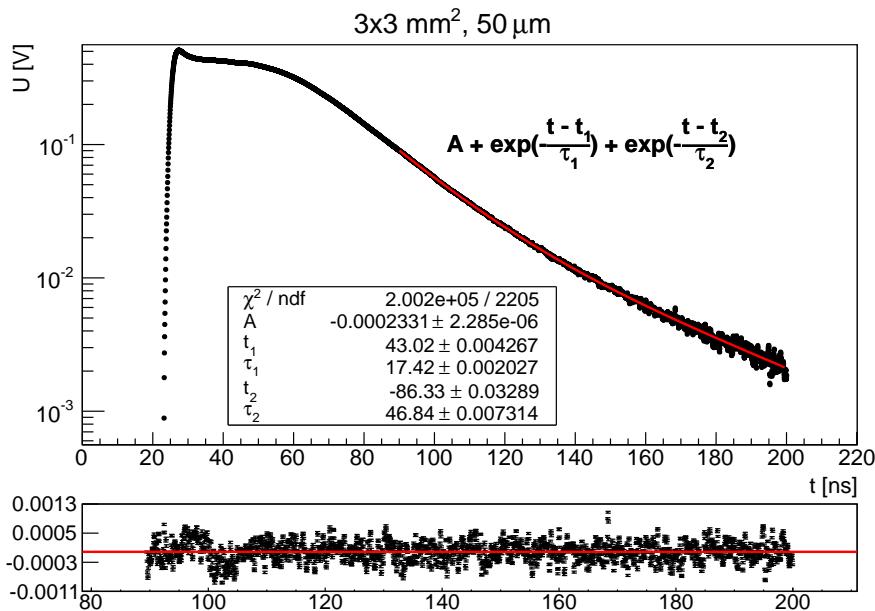
Figure B.13: Fit on the pulse tail of the $3 \times 3\,\mathrm{mm}^2$, $50\,\mu\mathrm{m}$ SiPM. The plotted SiPM pulse is the average of 200 pulses.
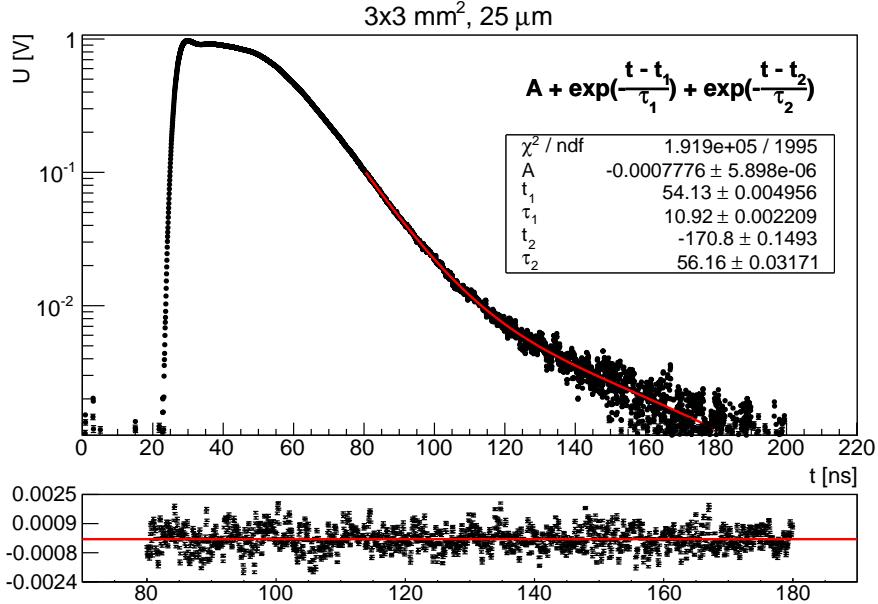
Figure B.14: Fit on the pulse tail of the $3 \times 3 \, \text{mm}^2$, $25 \, \mu\text{m}$ SiPM. The plotted SiPM pulse is the average of 200 pulses.
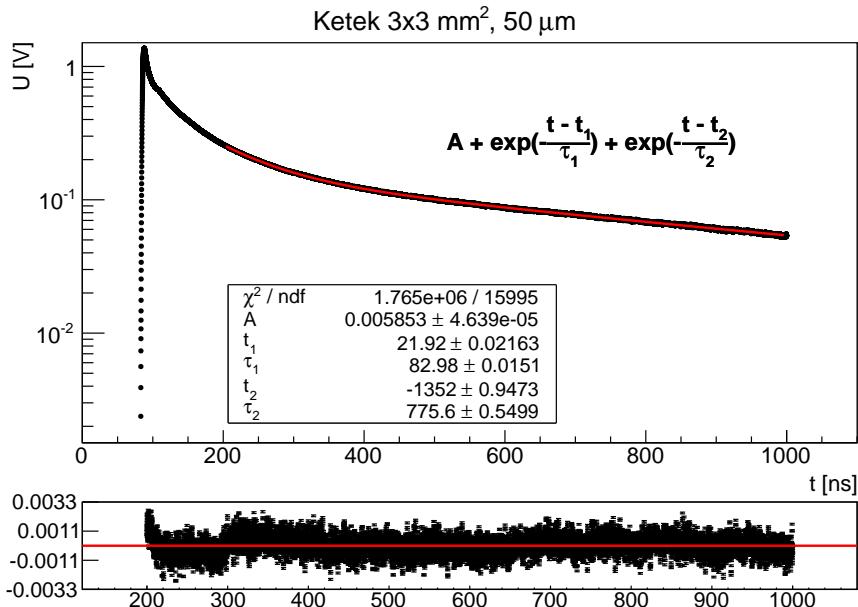
Figure B.15: Fit on the pulse tail of the KETEK $3 \times 3 \, \text{mm}^2$, $50 \, \mu\text{m}$ SiPM. The plotted SiPM pulse is the average of 200 pulses.

B.3. Absolute Pulse Height Ratio
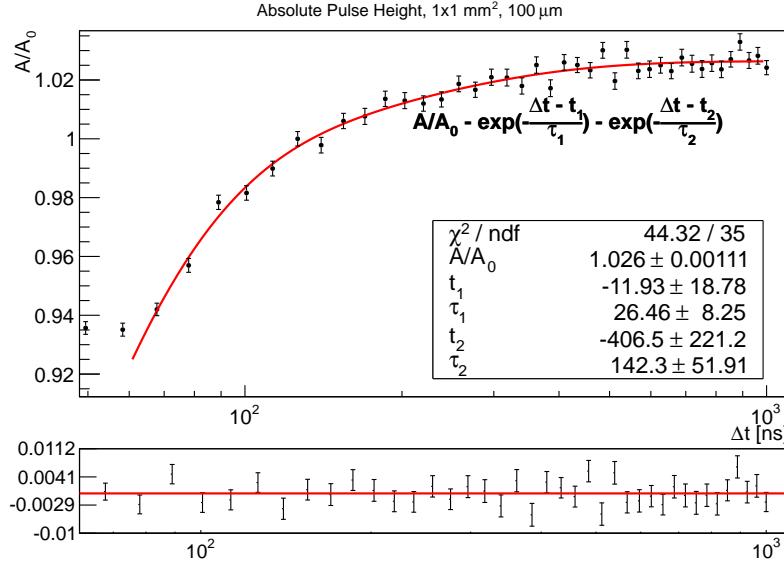
Figure B.16: Amplitude ratio of the $1 \times 1\,\text{mm}^2$, $100\,\mu\text{m}$ SiPM pulses with the fit of two superpositioned exponential functions.
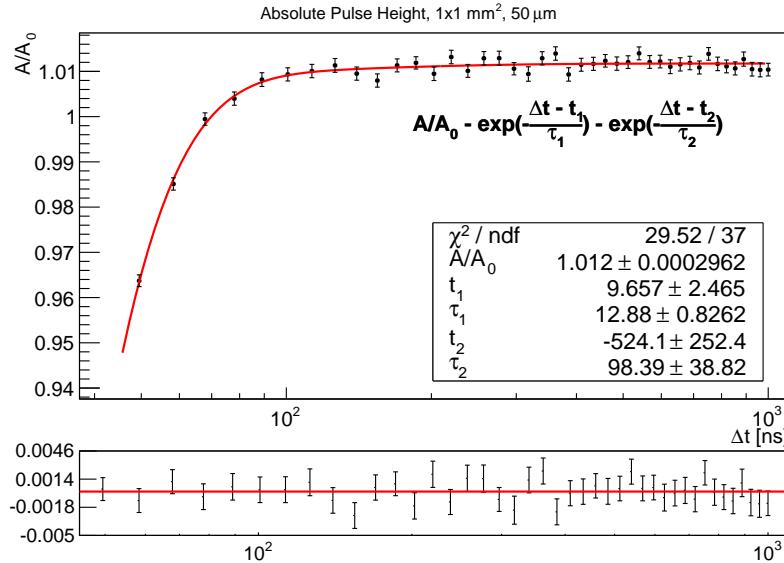
Figure B.17: Amplitude ratio of the $1 \times 1\,\text{mm}^2$, $50\,\mu\text{m}$ SiPM pulses with the fit of two superpositioned exponential functions.
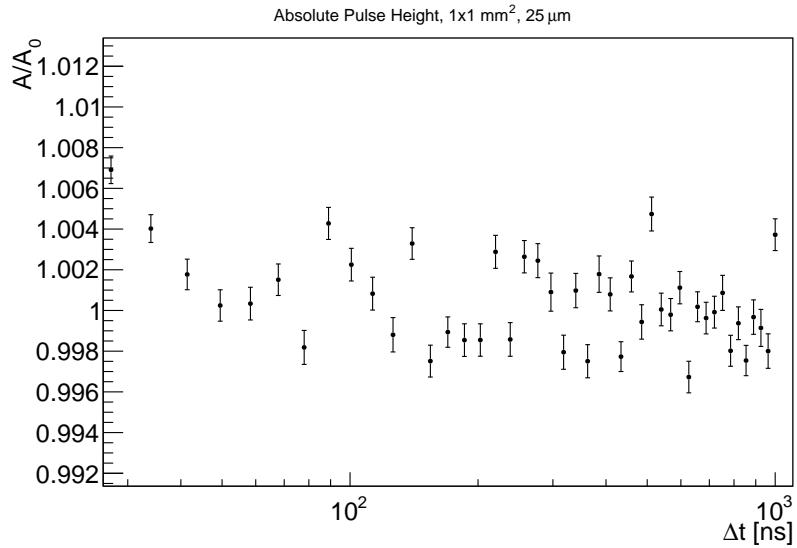
Figure B.18: Amplitude ratio of the $1 \times 1 \, \mathrm{mm}^2$, $25 \, \mu\mathrm{m}$ SiPM pulses.
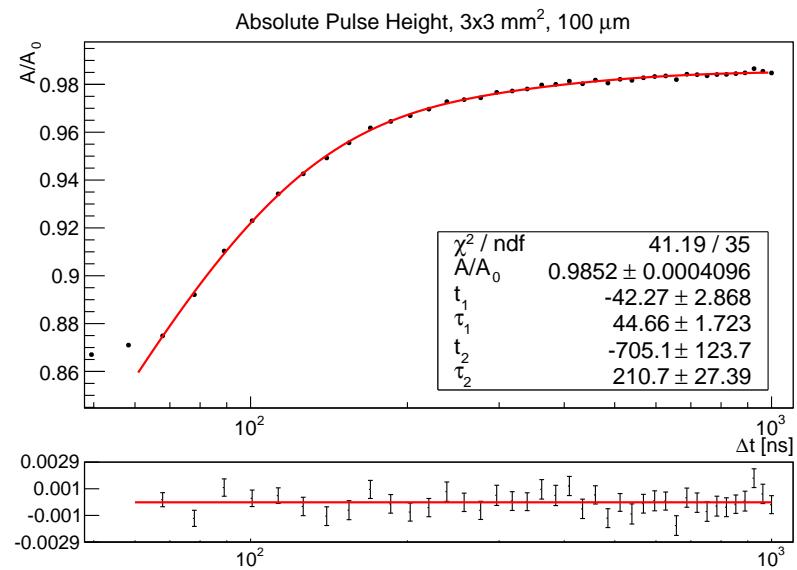
Figure B.19: Amplitude ratio of the $3 \times 3 \, \mathrm{mm}^2$, $100 \, \mu\mathrm{m}$ SiPM pulses with the fit of two superpositioned exponential functions.
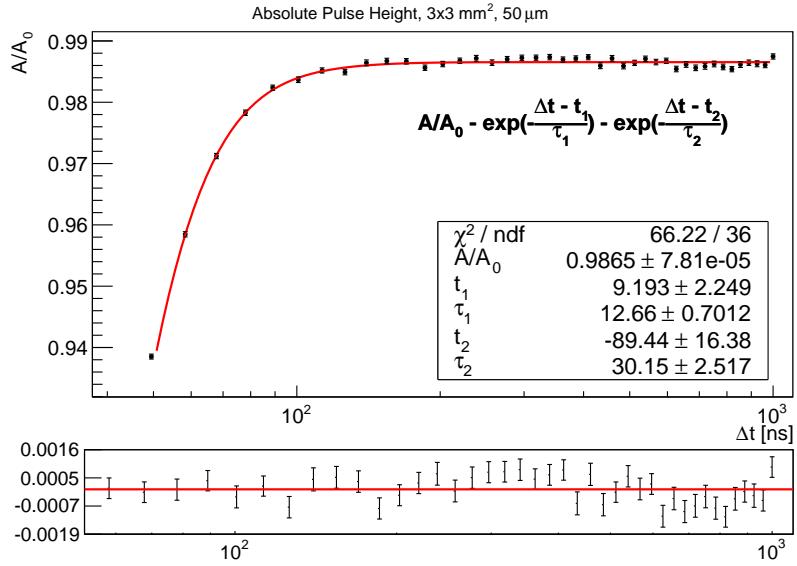
Figure B.20: Amplitude ratio of the $3 \times 3 \, \text{mm}^2$, $50 \, \mu\text{m}$ SiPM pulses with the fit of two superpositioned exponential functions.
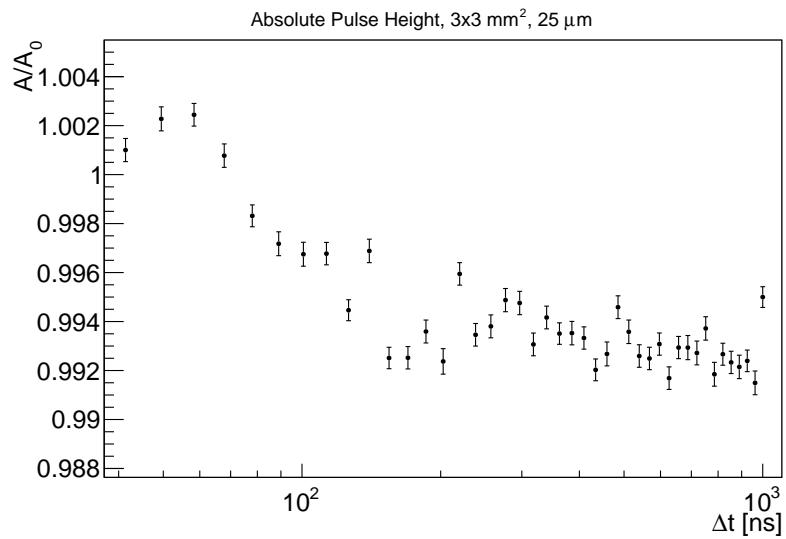

Figure B.21: Amplitude ratio of the $3 \times 3 \, \text{mm}^2$, $25 \, \mu\text{m}$ SiPM pulses.
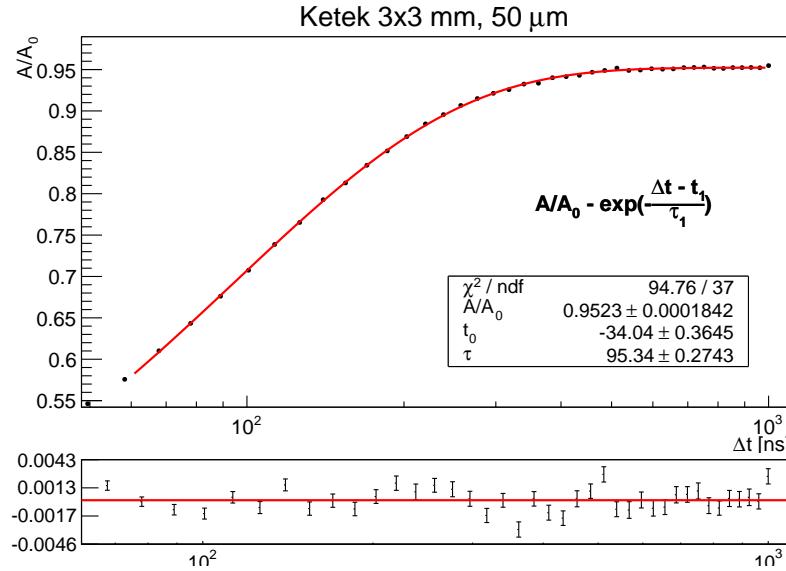
Figure B.22: Amplitude ratio of the KETEK $3 \times 3\,\text{mm}^2$, $50\,\mu\text{m}$ SiPM pulses with the fit of one exponential function. This is the only SiPM type where a considerable drop in the pulse height has been observed.

References

[1] S. M. Sze and Kwok K. Ng. *Physics of Semiconductor Devices*. John Wiley & Sons, Inc., New Jersey, 3rd edition, 2007.

[2] Gerhard Lutz. *Semiconductor Radiation Detectors*. Springer-Verlag, Berlin Heidelberg, 1st edition, 1999.

[3] D. Renker. Geiger-mode avalanche photodiodes, history, properties and problems. *Nuclear Instruments and Methods in Physics Research Section A: Accelerators, Spectrometers, Detectors and Associated Equipment*, 567(1):48–56, 2006.

[4] Holger Göbel. *Einführung in die Halbleiter-Schaltungstechnik*. Springer-Verlag, Berlin Heidelberg, 3rd edition, 2008.

[5] Wolfgang Demtröder. *Experimentalphysik 3: Atome, Moleküle und Festkörper*. Springer-Verlag, Berlin Heidelberg, 4th edition, 2010.

[6] J. R. Brews. Band-bending diagram for p-n-junction diode at zero bias. `http://en.citizendium.org/wiki/File:Pn-junction_zero_bias.PNG`, January 2011.

[7] S. Privitera, S. Tudisco, L. Lanzano, F. Musumeci, A. Pluchino, A. Scordino, A. Campisi, L. Cosentino, P. Finocchiaro, G. Condorelli, et al. Towards a new concept of photomultiplier based on silicon technology. *arXiv preprint arXiv:0705.0672*, 2007.

[8] I. Britvitch, Y. Musienko, and D. Renker. Investigation of a photon counting avalanche photodiode from Hamamatsu photonics. *Nuclear Instruments and Methods in Physics Research Section A: Accelerators, Spectrometers, Detectors and Associated Equipment*, 567(1):276–280, 2006.

[9] A. Stoykov, Y. Musienko, A. Kuznetsov, S. Reucroft, and J. Swain. On the limited amplitude resolution of multipixel Geiger-mode APDs. *Journal of Instrumentation*, 2:P06005, 2007.

[10] P. Buzhan, B. Dolgoshein, A. Ilyin, V. Kantserov, V. Kaplin, A. Karakash, A. Pleshko, E. Popova, S. Smirnov, Y. Volkov, et al. An advanced study of silicon photomultiplier. *ICFA Instrum. Bull*, 23:28–41, 2001.

[11] Hamamatsu. MPPC S10362 data sheet. `http://sales.hamamatsu.com/assets/pdf/parts_S/mppc_kapd0002e08.pdf`, September 2010.

References

[12] S. Seifert, H.T. van Dam, J. Huizenga, R. Vinke, P. Dendooven, H. Lohner, and D.R. Schaart. Simulation of silicon photomultiplier signals. *Nuclear Science, IEEE Transactions on*, 56(6):3726–3733, 2009.

[13] H. Otono, H. Oide, S. Yamashita, T. Yoshioka, K. Yamamoto, K. Yamamura, and K. Sato. Study of the internal mechanisms of Pixelized Photon Detectors operated in Geiger-mode. *Arxiv preprint arXiv:0808.2541*, 2008.

[14] V.M. Grebenyuk, A.I. Kalinin, N.M. Shat, AK Zhanusov, and VA Bednyakov. Simulation of the avalanche process in the G-APD and circuitry analysis of the SiPM. *Arxiv preprint arXiv:0903.1161*, 2009.

[15] K.A. Wangerin, G.C. Wang, C. Kim, and Y. Danon. Passive electrical model of silicon photomultipliers. In *Nuclear Science Symposium Conference Record, 2008. NSS'08. IEEE*, pages 4906–4913. IEEE, 2009.

[16] Carsten Heidemann. Simulations of the electrical model of SiPMs with SPICE. private communication, 2011.

[17] Y. Musienko. Advances in multipixel Geiger-mode avalanche photodiodes (silicon photomultipliers). *Nuclear Instruments and Methods in Physics Research Section A: Accelerators, Spectrometers, Detectors and Associated Equipment*, 598(1):213–216, 2009.

[18] P. Eckert, H.C. Schultz-Coulon, W. Shen, R. Stamen, and A. Tadday. Characterisation studies of silicon photomultipliers. *Nuclear Instruments and Methods in Physics Research Section A: Accelerators, Spectrometers, Detectors and Associated Equipment*, 620(2-3):217–226, 2010.

[19] Felix Bachmair. Verbesserung eines Flugzeitspektrometers zur Identifikation von Targetfragmenten für die Hadronentherapie. Diplomarbeit, III. Phys. Inst. B, RWTH Aachen University, July 2011.

[20] M. Stephan, T. Hebbeker, M. Lauscher, C. Meurer, T. Niggemann, and J. Schumacher. Future use of silicon photomultipliers for the fluorescence detection of ultra-high-energy cosmic rays. In *SPIE Optics + Photonic, San Diego, USA*, 2011.

[21] Markus Lauscher. private communication, 2011.

[22] I. Britvich and D. Renker. Measurements of the recovery time of Geiger-mode avalanche photodiodes. *Nuclear Instruments and Methods in Physics Research Section A: Accelerators, Spectrometers, Detectors and Associated Equipment*, A567:260–263, 2006.

[23] G. Bondarenko, P. Buzhan, B. Dolgoshein, V. Golovin, E. Guschin, A. Ilyin, V. Kaplin, A. Karakash, R. Klanner, V. Pokachalov, et al. Limited geiger-mode microcell silicon photodiode: new results. *Nuclear Instruments and Methods in Physics Research Section A: Accelerators, Spectrometers, Detectors and Associated Equipment*, 442(1-3):187–192, 2000.

References

[24] J. Barral. Study of silicon photomultipliers. `http://www.stanford.edu/~jbarral/Downloads/StageOption-Rapport.pdf`, 2004.

[25] Johannes Schumacher. Characterization studies of silicon photomultipliers: Noise and relative photon detection efficiency. Bachelor's thesis, III. Phys. Inst. A, RWTH Aachen University, February 2011.

[26] H. Oide, H. Otono, S. Yamashita, T. Yoshiota, H. Hano, and T. Suehiro. Study of afterpulsing of MPPC with waveform analysis. *PoS (PD07)*, 8, June 2007.

[27] P. Buzhan, B. Dolgoshein, L. Filatov, A. Ilyin, V. Kantzerov, V. Kaplin, A. Karakash, F. Kayumov, S. Klemin, E. Popova, et al. Silicon photomultiplier and its possible applications. *Nuclear Instruments and Methods in Physics Research Section A: Accelerators, Spectrometers, Detectors and Associated Equipment*, 504(1-3):48–52, 2003.

[28] E. Jones, T. Oliphant, P. Peterson, et al. SciPy: Open source scientific tools for Python. `http://www.scipy.org/`, 2001–2011.

[29] J. Nocedal and S.J. Wright. *Numerical optimization*. Springer-Verlag, 1999.

[30] K.B. Thei, H.M. Chuang, S.F. Tsai, C.T. Lu, and W.C. Liu. Characteristics of polysilicon resistors for sub-quarter micron CMOS applications. In *32th European Solid-State Device Research Conference*, September 2002.

[31] S.Y. Ko, J.S. Kim, G.H. Lim, and S.K. Kim. A new polysilicon resistor model considering geometry dependent voltage characteristics for the deep sub-micron CMOS process. In *Microelectronic Test Structures, 2006. ICMTS 2006. IEEE International Conference on*, pages 27–30. IEEE.

[32] Jörg Rennefeld. Studien zur Eignung von Silizium Photomultipliern für den Einsatz im erweiterten CMS Detektor am SLHC. Diplomarbeit, III. Phys. Inst. B, RWTH Aachen University, February 2010.

Devices

[33] HAMAMATSU, MPPC *S10362*, http://sales.hamamatsu.com/de/produkte/
     solid-state-division/si-photodiode-series/mppc.php.

[34] KETEK, SiPM Charge: *EMFT 5 - W9*, Type: *50G2*, http://indico.cern.ch/
     materialDisplay.py?contribId=23&sessionId=3&materialId=slides&confId=
     117424.

[35] THORLABS, LED *LED465E*, http://www.thorlabs.de/thorProduct.cfm?
     partNumber=LED465E.

[36] THORLABS, Integrating Sphere *IS200-4*, http://www.thorlabs.de/thorProduct.
     cfm?partNumber=IS200-4.

[37] HAMAMATSU, p-i-n Photodiode *S9195*, http://sales.hamamatsu.com/de/
     produkte/solid-state-division/si-photodiode-series/si-pin-photodiode.
     php.

[38] TEKTRONIX, Arbitrary Function Generator *AFG3252*, http://www.tek.com/
     products/signal-generator/afg3000/.

[39] KEITHLEY, Voltage Source *SourceMeter2400*, http://www.keithley.com/
     products/dcac/voltagesource/broadpurpose/?mn=2400.

[40] KEITHLEY, Picoammeter *6485*, http://www.keithley.com/products/dcac/
     sensitive/lowcurrent/?mn=6485.

[41] LECROY, Oscilloscope *WavePro 725Zi*, http://www.lecroy.com/oscilloscope/
     oscilloscopemodel.aspx?modelid=4717&capid=102&mid=504.

[42] THORLABS, Optical Multimode Fiber Cable, ⌀1 mm, NA 0.39 *M30L01*, http:
     //www.thorlabs.de/thorProduct.cfm?partNumber=M30L01.

Acknowledgements

First, I would like to thank Prof. Hebbeker for providing the opportunity to write my Bachelor's thesis at his institute. The last three month provided an insight into the fascinating and demanding life of a scientist. Thanks for this experience.

A special thank goes to Dr. Markus Merschmeyer, who had always time for me and who gave me many fascinating insights into silicon photomultipliers and particle detector development in general. I am very grateful for such well and individual supervision of my research and Bachelor's thesis. Thank you very much for all your advice and help.

A big thank goes to all my fellow SiPM researchers, who provided many useful suggestions and interesting discussions. This thesis wouldn't have been possible without their research.

I would also like to thank the whole CMS group at our institute for providing the inspiring opportunity to see behind the curtain of the search for new physics at the LHC. The discussions and inspirations in our weekly meetings helped me a lot.

I thank the Auger guys in my office for their advices concerning physics, ROOT and LaTeX. Also, thank you for the countless hours of fun while drinking coffee with you guys.

I would like to thank the whole 3rd Physical Institute for providing a great atmosphere and many fruitful discussions.

Another thank goes to Sebastian, who did proof reading of my thesis on short notice.

Last but not least I would like to thank my family and my girlfriend for their tremendous support. I apologize, for not having much time for you in the last three month.